

Enhanced pedestal transport driven by edge collisionality on Alcator C-Mod and its role in regulating H-mode pedestal gradients

M.A. Miller¹, J.W. Hughes¹, A.M. Rosenthal², S. Mordijck³, R. Reksoatmodjo⁴, M. Wigram¹, J. Dunsmore¹, F. Sciortino⁵, R.S. Wilcox⁶, T. Odstrčil⁷

¹MIT Plasma Science and Fusion Center, Cambridge, MA 02139, USA

²Commonwealth Fusion Systems, Devens, MA 01434, USA

³William & Mary, Williamsburg, VA 23188, USA

⁴Lawrence Livermore National Laboratory, Livermore, CA 94550, USA

⁵Proxima Fusion, 81671 München, Germany

⁶Oak Ridge National Laboratory, Oak Ridge, TN 37831, USA

⁷General Atomics, San Diego, CA 92186, USA

E-mail: millerma@mit.edu

Abstract. Experimental measurements of plasma and neutral profiles across the pedestal are used in conjunction with 2D edge modeling to examine pedestal stiffness in Alcator C-Mod H-mode plasmas. Enhanced D_α (EDA) experiments on Alcator C-Mod observed pedestal degradation and loss in confinement below a critical value of net power crossing the separatrix, $P_{\text{net}} = P_{\text{net}}^{\text{crit}} \approx 2.3$ MW, in the absence of any external fueling. New analysis of ionization and particle flux profiles reveal saturation of the pedestal electron density, n_e^{ped} , despite continuous increases in ionization throughout the pedestal, inversely related to P_{net} . A limit to the pedestal ∇n_e emerges as the particle flux, Γ_D , continues to grow, implying increases in the effective particle diffusivity, D_{eff} . This is well-correlated with the separatrix collisionality, ν_{sep}^* and a turbulence control parameter, α_t , implying a possible transition in type of turbulence. The transition is well correlated with the experimentally observed value of $P_{\text{net}}^{\text{crit}}$. SOLPS-ITER modeling is performed for select discharges from the power scan, constrained with experimental electron and neutral densities, measured at the outer midplane. The modeling confirms general growth in D_{eff} , consistent with experimental findings, and additionally suggests even larger growth in χ_e at the same $P_{\text{net}}^{\text{crit}}$.

1. Introduction

The physics that determine plasma profiles in the edge of tokamak plasmas remains among the most elusive in tokamak physics. It is known that at sufficient input power, a transition to a high-confinement mode (H-mode) occurs, resulting in a substantial reduction in edge transport, increasing pressure gradients, and forming the so-called “pedestal” [1]. It is well-known that achievable core pressures are very sensitive to the conditions at the boundary [2, 3, 4, 5, 6]. Next-generation devices [7, 8] seeking to maximize fusion gain rely on a robust edge pedestal. If the H-mode pedestal is to be exploited for high fusion gain, confidence in understanding the mechanisms determining its structure and the ability to form a desired type of pedestal must increase, especially in view of integrating this edge with a viable heat exhaust scrape-off layer (SOL) and divertor solution.

Some models have had reasonable success in predicting the pressure pedestal structure of H-modes exhibiting Type-I edge localized modes (ELMs) in conventional aspect ratio machines [9, 10, 11, 12]. Regardless, prediction of pedestal structure in turbulence-limited H-modes without ELMs is less certain [13]. Density pedestals in particular are especially poorly understood, largely as a result of a lack of edge ionization source measurements. It is unclear to what extent neutral fueling, as opposed to particle transport, is responsible for the build up of edge pedestal density gradients [14, 15]. Certain models suggest that the density pedestal width may be strongly linked to the

neutral penetration depth [16, 17]. While this may hold in some H-mode regimes, it cannot explain the width of all density pedestals [14, 18]. In ohmic L-modes, turbulent transport has been identified as important for regulating edge gradients [19, 20], and it is unknown to what degree turbulence is responsible for holding H-mode gradients at or near marginal stability. Since the very small length scales in the pedestal makes direct gyrokinetic simulation of these instabilities challenging, reduced-order models can serve as alternatives. Knowledge of the distribution of sources in the edge, in particular the ionization source, is an asset to testing reduced-order fueling and transport models.

It is also thought that understanding and predicting the density and temperature pedestals individually is crucial for differentiating between the different flavors of H-mode [21, 22]. The density at the edge in particular is a very important parameter for determining how particles and heat cross onto open field lines and affect the survivability of the divertor [23, 24].

Alcator C-Mod operated until 2016, and it routinely achieved the highest plasma densities of current tokamaks, fairly close to and often exceeding densities proposed for reactors [25, 26, 15]. As edge plasma density rises, opaqueness to neutrals increases, and fueling through gas puffing may become a challenge. As opaqueness increases, the ionization profile may move radially outward onto the unconfined plasma. If this is the case for future reactors, their ability to sustain large density gradients in the edge may be significantly reduced. A proposed metric for plasma opaqueness, $\eta = a \times n$, where a is the plasma

minor radius and n is the plasma density, puts Alcator C-Mod's opaqueness close to that expected on SPARC and ITER [15, 27]. Higher a and \bar{n}_e are thought to increase the difficulty with which an edge neutral can reach the core. Ionization profiles on Alcator C-Mod thus provide insight into how ionization could look in future devices. Furthermore, pedestal resiliency to fueling and evidence of critical edge gradients [18, 19] on C-Mod may be a feature of high-density devices with which future reactors need to contend.

To this end, this work attempts to study the structure of the density pedestal on Alcator C-Mod using edge ionization and plasma density measurements. From inferences of particle transport and high-resolution Thomson scattering measurements of pedestal structure, this paper finds particle transport, as well as heat transport, in the pedestal to be largely influential in determining critical edge gradients and the achievable pedestal densities in a number of H-modes on Alcator C-Mod.

This paper begins by outlining the set of diagnostics used to create a database of edge ionization and pedestal profiles. Section 3 then compares experimental ionization measurements with density measurements from a particular set of experiments at fixed magnetic field, plasma current, and plasma shape to make comments about observed pedestal stiffness, and the accompanying increase in particle transport. Section 4 then considers the pedestal operational space, and makes claims about how the C-Mod plasma moves around this operational space. It identifies collisionality, particularly at the edge, as a key driver for determining both the density and temperature pedestal. To supplement these experimental observations, Section 5 focuses on results from a set of simulations containing high-fidelity and experimentally-validated 2D calculations of the ionization source. The paper then ends with discussion on implications of these results for next-generation devices, and future steps that will be taken to develop a predictive model for next-generation density pedestals.

2. Experimental ionization and particle flux profiles in a set of magnetic balance experiments

In 2007, a series of experiments were performed on Alcator C-Mod to study the effect of switching the magnetic geometry from lower single null (LSN) to upper single null (USN) on the EDA H-mode regime. The EDA H-mode is a type of H-mode not limited by peeling-ballooning MHD modes, as the more typical type-I ELMing H-modes are [28, 21]. To study the effect of the magnetic drift on EDA H-mode pedestal quality, for a fixed toroidal magnetic field, $B_t = 5.4$ T, plasma current, $I_P = 0.8$ MA, and ∇B -drift direction, the active null was moved from the lower chamber to the upper chamber, effectively modifying the outer midplane distance between the separatrices passing through the two X-points, ΔR_{sep} , from around -5 mm to $+5$ mm. The current work focuses solely on plasmas solidly in LSN, with $\Delta R_{\text{sep}} \approx -5$ mm. These were all obtained at relatively fixed shape, with elongation, $\kappa \approx 1.6$, and triangularity, $\delta \approx 0.5$. They had a major radius, $R_0 \approx 0.67$

m and a minor radius, $a \approx 0.22$ m. Figure 1 shows a typical magnetic equilibrium for these plasmas, showing also views of the diagnostics to be described in Sections 2.2 and 2.3. As was the case for many H-modes on Alcator C-Mod, gas was only injected in the L-mode phase, and the target density was sustained in the H-mode without any additional gas request on the controller. These plasmas also received no external impurity injection.

This paper presents a self-consistent analysis of particle and neutral pedestal transport from these experiments. It does so by combining radially-resolved edge electron density and temperature (n_e , T_e) measurements from Thomson Scattering (TS) with measurements of neutral emissivity from a Lyman- α camera, $\epsilon_{\text{Ly}\alpha}$, to infer neutral density, n_0 , ionization source, S_{ion} , radial particle flux, Γ_D , and effective diffusivity, D_{eff} .

Shot= 1070821003 Time= 1.360 Ip = 0.79

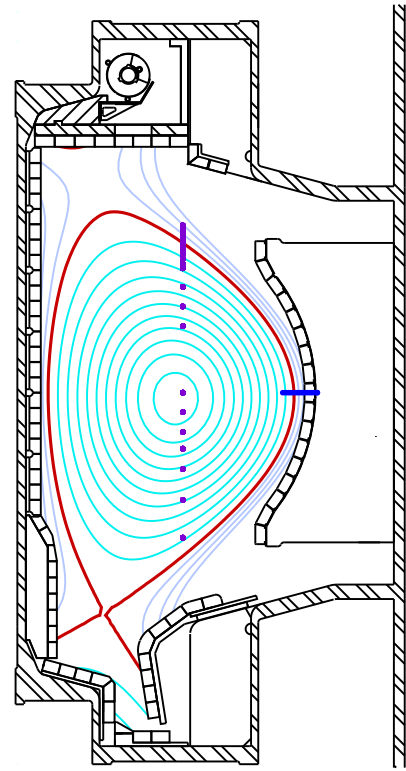


Figure 1: Typical magnetic equilibrium for LSN discharges in effective power scan. The thick red line demarcates the last closed flux surface, separating the closed field lines, shown in cyan, and the open field lines, shown in dark blue. The TS system in purple views vertically down the plasma. The sparser core system views across the majority of the core plasma. The edge TS system (ETS) views the area around the separatrix, located poloidally near the crown of the plasma in the LSN configuration. The LYMID system, shown in bright blue, is located exactly at the midplane and views toroidally along 20 chords.

2.1. Pedestal degradation with net power

It was observed that these plasmas, particularly their pedestals, were highly sensitive to variation in the net power

flowing through the scrape-off layer, P_{net} , calculated using $P_{\text{net}} = P_{\text{loss}} - P_{\text{rad}}$, where the loss power $P_{\text{loss}} = P_{\text{oh}} + P_{\text{aux}} - dW/dt$ and P_{rad} is the power radiated in the core. Auxiliary power P_{aux} in this case is just the total injected ion cyclotron range of frequencies (ICRF) power, P_{RF} . P_{oh} is the ohmic power, and dW/dt is the time derivative of the stored energy, W_{MHD} .

Figure 2 shows an effective scan in P_{net} from 1.3 MW to 3.4 MW. It shows large changes to many quantities in these discharges as P_{net} approaches and crosses a critical value of P_{net} , $P_{\text{net}}^{\text{crit}} \approx 2.3$ MW. The left panel of Figure 2 shows that the line-integrated density, \bar{n}_e , drops by $\sim 8\%$, simultaneous with large increases in W_{MHD} , the maximum normalized pressure gradient, α_{MHD} , and the normalized confinement factor, $H_{98,y2}$ (H_{98}) [29]. Recalling the expression for the opaqueness heuristic introduced in Section 1, the plot of \bar{n}_e also gives information about the opaqueness in these shots. Multiplying \bar{n}_e by a for these shots gives a range in opaqueness from $5.5 - 6.8 \times 10^{19} \text{m}^{-2}$. While these values are among the highest of current devices, they are not the highest achieved on C-Mod. For example, plasmas in the final campaigns of C-Mod achieved opaqueness values of up to $1.1 \times 10^{20} \text{m}^{-2}$ [30]. For reference, recent plasmas with Greenwald fraction larger than unity on DIII-D achieved an opaqueness just under $4.4 \times 10^{19} \text{m}^{-2}$ [31]. ITER and SPARC, on the other hand, are expected to operate at opaqueness values of $2.2 \times 10^{20} \text{m}^{-2}$ and $1.7 \times 10^{20} \text{m}^{-2}$, respectively [32, 6]. If instead, the plasma density is taken as $n = \frac{1}{2}(n_e^{\text{sep}} + n_e^{\text{ped}})$, as suggested in [15], the opaqueness for these discharges ranges from $3.1 - 4.3 \times 10^{19} \text{m}^{-2}$ and that predicted for SPARC and ITER are $1.6 \times 10^{20} \text{m}^{-2}$ and $1.5 \times 10^{20} \text{m}^{-2}$, respectively [33, 34].

The center panel of Figure 2 shows changes in pedestal plasma parameters as measured by the ETS diagnostic, outlined in Section 2.3. There is a large drop in the collisionality at $\psi_n = 0.95$, ν_{95}^* , resulting from a very slight drop in n_e^{ped} , but a large rise in T_e^{ped} . Each of these pedestal quantities is computed at their respective pedestal top, defined by the fit function described in Section 2.3 rather than at a particular flux surface. In general, these are at different locations for n_e and T_e . The bottom plot of the center panel differentiates, with color, discharges that are at high values of $\nu_{95}^* > 2$ and low values of $\nu_{95}^* < 2$. This transition in collisionality occurs at around a value of $P_{\text{net}} \approx 2.3$ MW, at which point all the quantities in Figure 2 show clear changes.

Revisiting this particular experiment through inspection of edge ionization profiles reveals the role of plasma transport in regulating the pedestal and thus, the H-mode quality. The right panel of Figure 2 alludes to this, showing large drops in the inferred n_0 , S_{ion} , Γ_D , and D_{eff} , all at the top of the pedestal. The discharges used in this dataset are the following: 10708210[03/04/05/08/09/12/13/20/21/22/23/25/29].

2.2. Neutral emissivity from Ly_α camera

Radial profiles of n_0 , S_{ion} , Γ_D , and D_{eff} are reconstructed from a midplane Ly_α camera called LYMID, using the

methodology outlined in Section 2.4. The camera was installed in 2007 as the successor to an earlier Ly_α system [35, 36]. It was located just below the midplane ($Z = -0.04$ m) and consisted of toroidal views. Its 20 chords were tangent to flux surfaces covering a region in the radial direction of just over 5 cm at the plasma edge. The LYMID diagnostic collected Ly_α light from the 121.6 nm vacuum ultra-violet light transition from the edge population of neutral deuterium atoms. This LYMID diagnostic recorded line-integrated brightness measurements from each of its viewing chords as a function of their tangency radius. We use the same tomographic inversion algorithm developed for LLAMA, a similar system on DIII-D [37, 38] to invert the brightness profile. This yields $\epsilon_{\text{Ly}_\alpha}$ as a function simply of radius, and no longer of toroidal angle, under the assumption of axisymmetric emission. No radial shift is applied to $\epsilon_{\text{Ly}_\alpha}$. Instead, an error associated with the magnetic reconstruction is included, as delineated at the end of Section 2.4.

2.3. Edge Thomson scattering for plasma profile analysis

In addition to neutral emissivity measurements, we use the ETS diagnostic, which was routinely used to diagnose the edge plasma, and in particular, the pedestal, on C-Mod. ETS measured both n_e and T_e in a region spanning 3 cm of the plasma edge. Measurements were located in the upper chamber near the crown of LSN plasmas, and could diagnose n_e and T_e profiles with order millimeter resolution when mapped to the midplane [39]. In order to estimate gradients as well as to facilitate interpolation onto the radial coordinate basis of the neutral emissivity profile, a fit to both n_e and T_e is applied. It was determined that a hyperbolic tangent as in [40], but supplemented with polynomial terms to allow for flexibility in adjusting the gradient inside the pedestal and in the SOL, was appropriate to fit the plasma data. Equation 1 shows the functional form of the modified hyperbolic tangent (mtanh).

$$y(z) = \frac{1}{2} [h + b + (h - b) \frac{P_1(z)e^z + P_2(z)e^{-z}}{e^z + e^{-z}}] \quad (1)$$

$P_1(z) = 1 + C_1z + C_2z^2 + C_3z^3$ and $P_2(z) = 1 + S_1z + S_2z^2$ are the core and SOL polynomials respectively, $z = 2\frac{x_0 - x}{\Delta}$ is the pedestal coordinate as a function of x , an arbitrary midplane coordinate, and h and b are the height and bottom of the pedestal, respectively. x_0 is the pedestal center, Δ is the pedestal width, C_1 , C_2 , and C_3 are the linear, quadratic, and cubic coefficients of the core polynomial, and S_1 and S_2 are the linear and quadratic coefficients of the SOL polynomial. Setting $C_2 = C_3 = S_1 = S_2 = 0$ recovers the form of the fit function used in [40]. Since the mtanh has a closed form, the n_e and T_e gradients (∇n_e and ∇T_e) can be computed analytically using the fit coefficients.

For ETS, we use the two-point model [41] to align n_e and T_e relative to the separatrix, $\psi_n = 1$. This model assumes that the power carried by the electrons in the SOL leaves the core entirely at the outer midplane and is

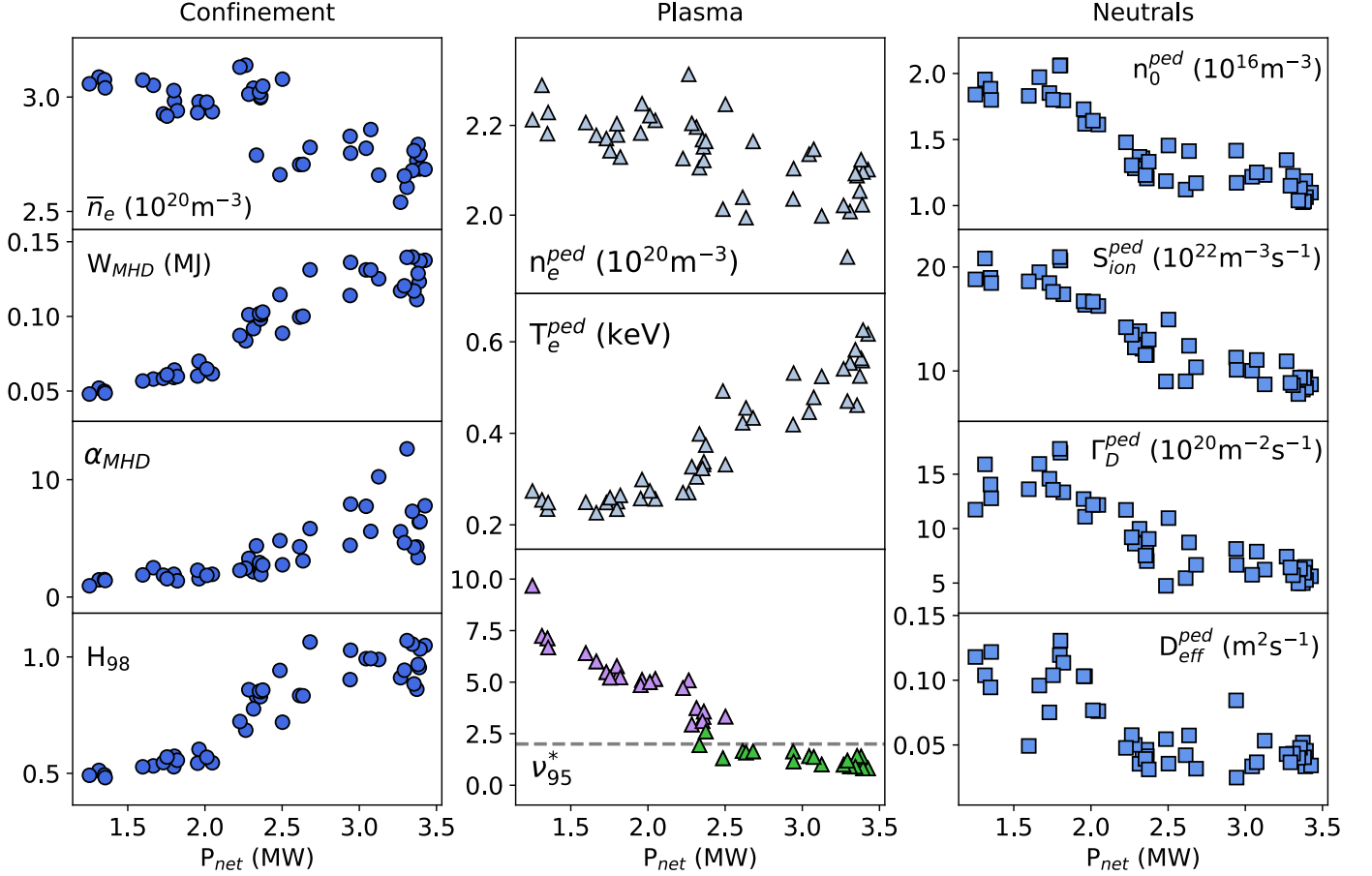


Figure 2: Various experimentally-determined quantities plotted against P_{net} . The plots in the left panel show quantities typically linked with plasma confinement in dark blue circles. The center panels show variation of plasma quantities at the pedestal top in gray triangles, with the exception of the bottom panel, showing collisionality at $\psi_n = 0.95$, for which a distinction in color is made. Purple triangles have $\nu_{95}^* > 2$, while green triangles have $\nu_{95}^* < 2$. This transition value roughly coincides with a critical value of $P_{\text{net}} \approx 2.3$ MW, at which all other quantities exhibit step-like changes. Finally, the panel on the right shows variation in quantities directly related to neutrals using light blue squares.

transported to the divertor target via conduction only. It uses the Spitzer-Härm conductivity, which is proportional to the parallel temperature gradient in the SOL. Hence, the equality,

$$-\frac{2}{7}\kappa_{0,e}\frac{\partial T_e^{7/2}}{\partial x_{\parallel}} = \frac{\frac{1}{2}P_{\text{net}}}{2\pi R\lambda_q\frac{B_{\theta}}{B}} \quad (2)$$

can be integrated to find T_e^{sep} at the outer midplane (OMP) [41]. In this equation, $\kappa_{0,e}$ is the Spitzer-Härm conductivity, R is the plasma major radius, λ_q is the width of the heat flux channel, B_{θ} is the poloidal magnetic field. In the absence of measurements of the parallel heat flux width, we use the Brunner scaling for λ_q [42]. We further assume negligible temperature at the divertor (i.e. $T_{e,\text{target}}^{7/2} \ll T_{e,\text{OMP}}^{7/2}$), as some target data available for these discharges indicate that $T_{e,\text{target}}$ does not typically exceed 25 eV for even the highest values of P_{net} . We also estimate the connection length required for the integral as $L_{\parallel} = q_{95}\pi R$, where q_{95} is the safety factor at the 95% flux surface. Finally, the factor of $\frac{1}{2}$ in front of P_{net} represents the assumption that half of the power crossing the separatrix is carried by the electrons (and half by the

ions), an assumption that will be discussed further in the modeling setup in Section 5. With $T_{e,\text{OMP}}^{\text{sep}}$ in hand, we find the radial shift required to align the fit to the T_e profile at $\psi_n = 1$ and apply the same shift to n_e before using these shifted kinetic profiles to calculate the rate coefficients used for the neutral inferences.

2.4. Inference of neutral density, ionization source, and particle flux

With n_e , T_e , and $\epsilon_{\text{Ly}\alpha}$ all mapped to the midplane, we make use of a collisional-radiative model to infer n_0 , S_{ion} , Γ_D , and an effective transport coefficient, D_{eff} . A similar procedure has been employed previously, on C-Mod with D_{α} measurements [14], and on both C-Mod and DIII-D with $\text{Ly}\alpha$ [19, 23, 43, 44, 45]. Equations 3 - 6 summarize the procedure for calculating these quantities.

$$n_0 = \frac{\epsilon_{\text{Ly}\alpha}}{\mathcal{P}(n_e, T_e)n_e} \quad (3)$$

$$S_{\text{ion}} = S_H(n_e, T_e)n_0n_e = \epsilon_{\text{Ly}\alpha}\frac{\mathcal{S}(n_e, T_e)}{\mathcal{P}(n_e, T_e)} \quad (4)$$

Table 1: Ranges of values at the location of the top of the n_e pedestal and at the separatrix for the discharges analyzed. n_e and T_e vary substantially at the separatrix, but T_e primarily varies at the pedestal top. In contrast, all neutral quantities vary substantially across discharges and at both the pedestal and the separatrix.

Parameter	n_e pedestal top	Separatrix
n_e (10^{20} m^{-3})	1.9 – 2.3	0.7 – 1.9
T_e (eV)	210 – 670	80 – 150
n_0 (10^{16} m^{-3})	1.0 – 2.1	1.9 – 4.3
S_{ion} ($10^{22} \text{ m}^{-3}\text{s}^{-1}$)	7.8 – 21	9.3 – 23
Γ_D ($10^{20} \text{ m}^{-2}\text{s}^{-1}$)	4.7 – 18	8.2 – 22
D_{eff} (m^2s^{-1})	0.025 – 0.13	0.016 – 0.11

$$\Gamma_{D,\perp}(r) = \int_0^r S_{\text{ion}}(r') dr' \quad (5)$$

$$D_{\text{eff}} = \frac{\Gamma_{D,\perp}}{|\nabla n_e|} \quad (6)$$

\mathcal{P} is the photon emissivity coefficient, $S_H = \frac{\mathcal{S}}{\mathcal{P}}$ is the ratio between \mathcal{S} , the effective ionization coefficient, and \mathcal{P} , the photon emissivity coefficient. Neutral and ionized molecular contributions are negligible for Ly_α emission. These expressions highlight the implicit dependence of S_{ion} (and hence $\Gamma_{D,\perp}$) on n_e and T_e .

Equations 3 and 4 use a number of simplifying assumptions about the relevant atomic processes, which are outlined in [44]. For Equation 5, we ensure a stationary plasma density time window and assume no poloidal asymmetries in S_{ion} , allowing computation of the cross-field particle flux, $\Gamma_{D,\perp}$ by integrating Equation 4 in a slab geometry. For the remainder of the paper, we drop the \perp subscript and express the cross-field particle flux as Γ_D . The assumption that there is negligible poloidal asymmetry in S_{ion} is likely the strongest simplifying assumption. Using two distinct Ly_α views, an in-out poloidal asymmetry has been observed in the ionization source on DIII-D [44, 46]. LYMID does not distinctly view the inboard and outboard side, and an in-out source asymmetry may well be present on C-Mod as well. Regardless, past work has shown that C-Mod is dominated by main-chamber fueling [47, 23]. This lends confidence to using neutral inferences at the midplane to make conclusions about fueling and transport in the C-Mod pedestal. We test this assertion with EIRENE, a 3D neutral simulation code, described in Section 5, and observe good agreement with previous conclusions about main chamber fueling.

Figure 3 shows typical profiles produced with this workflow. The panel on the left shows n_e and T_e measured by ETS as well as profile fits using Equation 1. The right panel of the figure shows n_0 , S_{ion} , Γ_D , and D_{eff} , all computed from a combination of data from LYMID and ETS. Note that given the non-negligible contribution to ionization from parallel particle flux, $\Gamma_{D,\parallel}$, in the SOL, we only calculate Γ_D and D_{eff} for $\psi_n \leq 1$. Table 1 summarizes the range in values for these profiles both at the pedestal

top, defined as the point $\Delta/2$ radially inward of the center of the mtanh profile, where Δ is the width of the mtanh (as well as the pedestal). Only the radial location at the top of the n_e pedestal is shown. Tabulated as well are values at the separatrix.

Uncertainties in the profiles in Figure 3 have been computed by perturbing the experimental data points, refitting and recomputing associated quantities multiple times, and then computing statistics on the fits. The perturbations to the experimental points are sampled from a Gaussian distribution with a half-width equal to the experimental uncertainty of the ETS data point. This process is repeated N times and the uncertainty is set to the standard deviation of the ensemble of N perturbed fits. Through sensitivity analysis, it was determined that $N = 100$ represented a good compromise between computational time and representation of the uncertainty. This technique enables uncertainty estimation not only in the absolute n_e and T_e profiles, but also in their gradients, as well as the neutral quantities computed from the plasma profiles. Furthermore, like proper weighted least squares including off-diagonal terms, this uncertainty estimation technique accounts for covariance between fit parameters. The technique is described in greater detail in [45].

As indicated earlier, we do not apply a shift to $\epsilon_{\text{Ly}_\alpha}$, as the measurement is made at the midplane and there is no model to constrain the measurement relative to the separatrix. To account for this uncertainty, we compute an error associated with uncertainty in the position of the separatrix as indicated by the magnetic reconstruction computed with EFIT, $\Delta R_{\text{EFIT}} = 2 \text{ mm}$. We thus estimate the error in $\epsilon_{\text{Ly}_\alpha}$ from LYMID, $\Delta \epsilon_{\text{Ly}_\alpha}$, by multiplying ΔR_{EFIT} by the radial derivative of the emissivity profile, $\frac{\partial \epsilon_{\text{Ly}_\alpha}}{\partial r}$, computed numerically, i.e. $\Delta \epsilon_{\text{Ly}_\alpha} = \Delta R_{\text{EFIT}} \frac{\partial \epsilon_{\text{Ly}_\alpha}}{\partial r}$. This error is then added in quadrature to the quantities computed from Equations 3 – 6.

3. Density pedestal stiffness

3.1. The role of ionization in the pedestal

We use this methodology to interrogate the role of pedestal ionization in influencing the electron density pedestal height. Figure 4 shows n_e plotted against S_{ion} at the separatrix, $S_{\text{ion}}^{\text{sep}}$. At low values of separatrix ionization, $S_{\text{ion}}^{\text{sep}} \lesssim 15 \times 10^{22} \text{ m}^{-3}\text{s}^{-1}$, n_e varies weakly with ionization at the pedestal top and perhaps more strongly at the separatrix. As S_{ion} continues to grow past $S_{\text{ion}}^{\text{sep}} = 15 \times 10^{22} \text{ m}^{-3}\text{s}^{-1}$, however, the trends diverge significantly. At the separatrix, n_e continues to increase with S_{ion} , while at the pedestal top there is clear insensitivity of the n_e pedestal height to the ionization source. These EDA H-modes settle at a natural density of $n_e^{\text{ped}} \approx 2.2 \times 10^{20} \text{ m}^{-3}$. Pedestal stiffness on Alcator C-Mod has been observed previously and may be a feature of high density EDAs [18]. In that work, it was shown that varying the neutral source through external gas puffing had little effect on gradient scale lengths in the pedestal as well as the pedestal height. Though similar phenomenology is observed here, a key difference

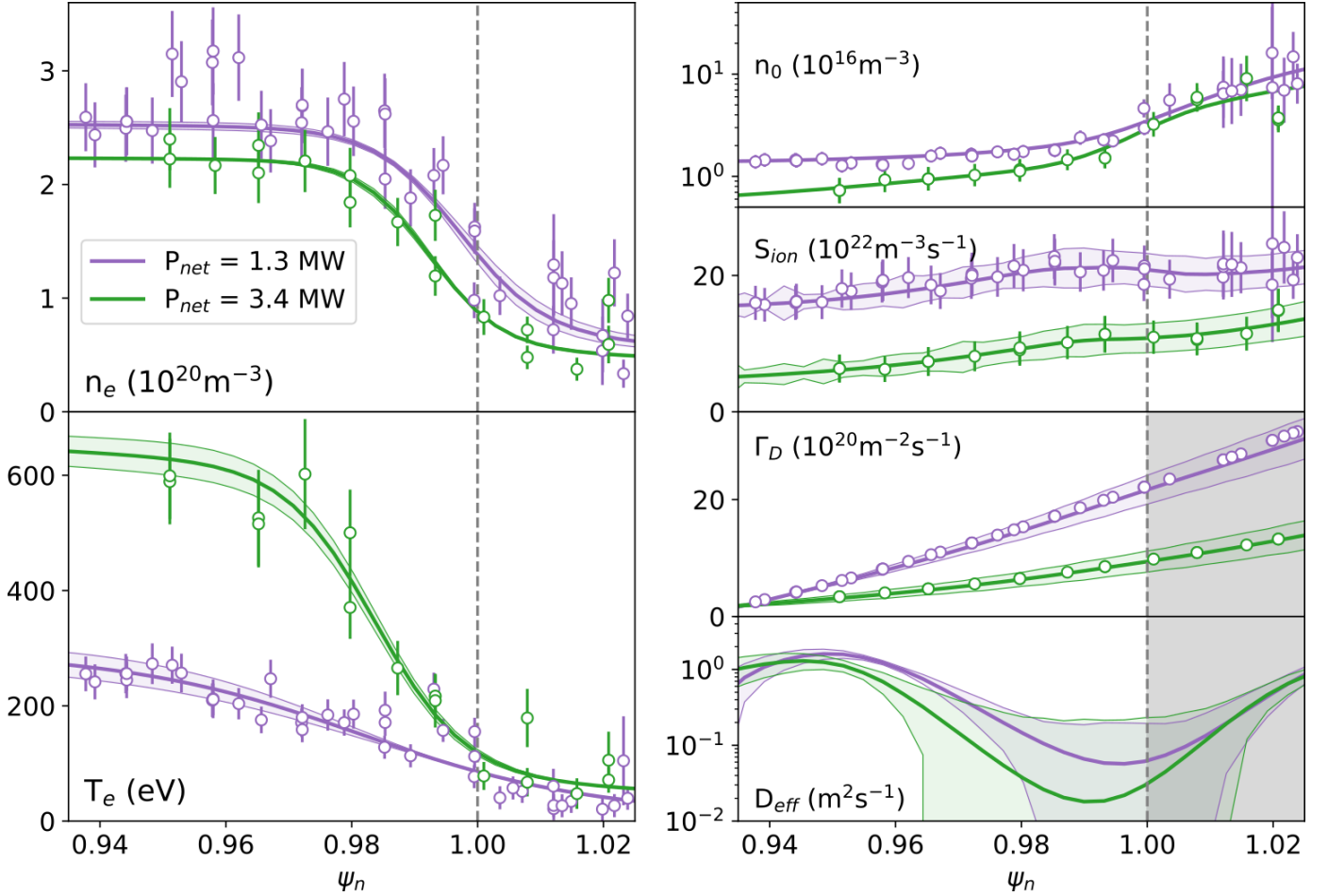


Figure 3: Typical kinetic profiles as measured by ETS and a combination of LYMID and ETS measurements. The left panel shows profiles from ETS, with n_e (top) and T_e (bottom). Shown as open circles are the raw ETS points, including measurement uncertainties. Thick solid lines represent profile fits using the modified hyperbolic tangent fit as described in Section 2.3. Thinner solid lines and the shaded region they envelop represent uncertainties in the fit procedure, as outlined in the same section. The right panel shows those from combined ETS and LYMID analysis. From top to bottom are n_0 , S_{ion} , Γ_D , and D_{eff} . The profiles in purple are at higher collisionality (higher n_e and lower T_e), the relevance of which is explained in Section 4. The ones in green are at lower collisionality (lower n_e and higher T_e). The dotted vertical line in gray denotes the separatrix, located at $\psi_n = 1.0$. As mentioned in the text, Γ_D and D_{eff} are only valid up to the separatrix. The profiles shown here correspond to cases simulated using SOLPS-ITER, described in Section 5.

is that the H-modes currently analyzed received no external gas puffing after the L-H transition. Once the H-mode was achieved, pedestal fueling occurred solely through recycled neutrals. Pedestal stiffness in opaque plasmas may thus occur naturally, even in the absence of active gas fueling.

3.2. Flux-gradient relationship in stiff profiles

It has often been assumed that S_{ion} determines n_e [17, 16]. With this framework, we might expect Γ_D , the integral of S_{ion} , to be proportional to the gradient in the density. In other words, Γ_D and ∇n_e would be linearly dependent, just as in a classical Fickian diffusive system. Figure 5, however, shows that the experimentally inferred Γ_D from the Ly α camera, calculated at the top of the pedestal does not grow linearly with ∇n_e at the same location. For $\nabla n_e \approx -150 \times 10^{20} \text{ m}^{-4}$, Γ_D can vary significantly, anywhere from $6 \times 10^{20} \text{ m}^{-2}\text{s}^{-1}$ to $16 \times 10^{20} \text{ m}^{-2}\text{s}^{-1}$. This is not surprising, given the saturation of n_e^{ped} for vastly different S_{ion} shown

in Figure 4.

Figure 5 indicates that there may be a particular gradient beyond which further ionization becomes ineffective in modifying the density profile, yielding a stiff pedestal. The peak ∇n_e occurs in the mid-range of Γ_D values, at $\sim 10 \times 10^{20} \text{ m}^{-2}\text{s}^{-1}$. This is consistent with the rapid growth of n_e^{sep} at fixed n_e^{ped} shown in Figure 4. Discharges at low Γ_D^{ped} correspond to those at low S_{ion}^{sep} and low n_e^{sep} . Those at mid Γ_D^{ped} and largest ∇n_e^{ped} correspond to discharges at $S_{ion}^{sep} \approx 15 \times 10^{22} \text{ m}^{-3}\text{s}^{-1}$ and intermediate n_e^{sep} . Finally, the discharges at high Γ_D^{ped} but reduced ∇n_e^{ped} (relative to those at mid Γ_D^{ped}) correspond to those at highest S_{ion}^{sep} . These are the discharges with increasing n_e^{sep} but nearly fixed n_e^{ped} . Generally also, discharges at low S_{ion} and low Γ_D correspond to those at high P_{net} and vice versa, as suggested by Figure 2.

It is evident that these pedestals cannot be fully described with a purely diffusive transport model of

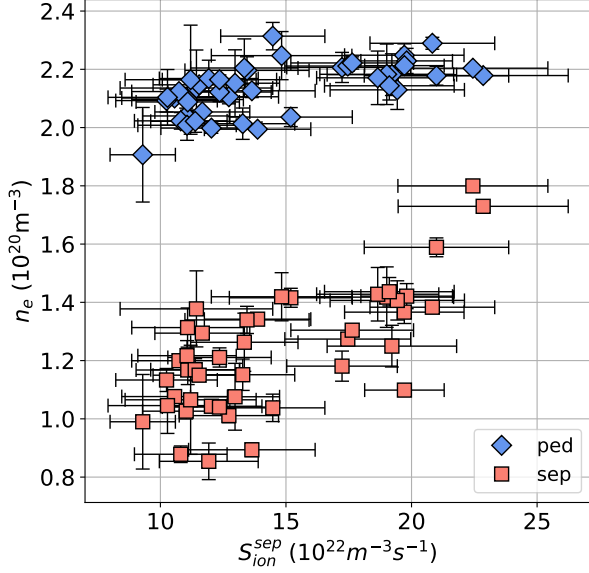


Figure 4: Electron density plotted against volumetric neutral ionization rate at the outer midplane at the separatrix (light red squares) and at the top of the n_e pedestal (light blue diamonds). While n_e^{sep} continues to increase as $S_{\text{ion}}^{\text{sep}}$ does, n_e^{ped} does not beyond a value of $n_e^{\text{ped}} \approx 2.35 \times 10^{20} \text{ m}^{-3}$.

constant D . Since S_{ion} , and thus Γ_D , varies significantly at relatively constant n_e^{ped} , it is unlikely that just adding a convective term, proportional to n_e^{ped} , to the transport model might explain the large changes to Γ_D in these pedestals. Instead, it could be that a threshold based model, like that describing heat transport near critical gradients in the core [48], may be necessary for understanding pedestal particle transport. Such a phenomenon in the particle channel has been previously suggested on Alcator C-Mod in the near-SOL for ohmic L-modes [19] and in the pedestal of EDA H-modes undergoing strong puffing [18].

In the absence of such a model, we opt for using the quotient of the inferred particle flux and the density gradient to obtain an effective particle diffusivity, D_{eff} , calculated using Equation 6. While not fully descriptive of the physics of the edge, D_{eff} provides a point of comparison for analyzing differences in transport between discharges and as a function of different edge conditions. Experimental inferences of D_{eff} have been previously made on C-Mod using Γ_D inferred from the workflow in Section 2.4 [14, 23], although never within the pedestal with both LYMID and ETS simultaneously. An important caveat of this steady-state analysis is that in using a single coefficient, one cannot distinguish different types of particle transport, as becomes possible using time-dependent analysis. On DIII-D, for example, recent experiments have sought to calculate both a diffusive coefficient, D , and a convective velocity coefficient, v , simultaneously using LLAMA [44]. To do this requires perturbing the edge slightly so as to recover $\frac{\partial n}{\partial t}$ without substantially changing the intrinsic transport properties.

For these stationary discharges, we opt for D_{eff} , and

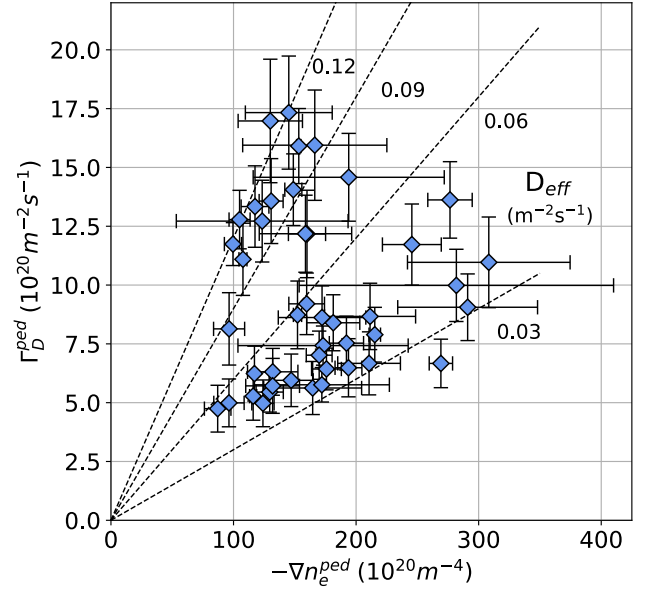


Figure 5: Particle flux at the top of the pedestal plotted against density gradient at the same location. Even at large Γ_D , $-\nabla n_e$ does not increase much past $300 \times 10^{20} \text{ m}^{-4}$. The dashed lines show different slopes, corresponding to different values of D_{eff} . The points lie at a large range of D_{eff} , indicating inconsistency with a diffusive transport model using a constant D .

add lines of constant D_{eff} to Figure 5 to demonstrate the large variation in this proxy for transport in these plasmas. As shown in the rightmost panel of Figure 2 and now apparent from Figures 4 and 5, the rapid growth in S_{ion} and Γ_D at low P_{net} , as well as the saturation of n_e^{ped} , occurs along with a rapid growth of $D_{\text{eff}}^{\text{ped}}$ below the critical value of $P_{\text{net}} \approx 2.3 \text{ MW}$.

4. Pedestal operational space and transport drive

Particle transport and fueling depend on and affect T_e as well as n_e . Neutral transport resulting from atomic processes has a strong dependence on T_e , and intrinsic changes to plasma transport modify and are modified by kinetic profiles, including T_e [14, 15]. Figure 3 shows characteristic n_e and T_e pedestal profiles at low and high P_{net} , shown in green and purple respectively. There is a clear drop in T_e^{ped} at low P_{net} . Figure 6 shows the phase space of these plasmas in terms of n_e and T_e , at $\psi_n = 0.95$, (n_e^{95} , T_e^{95}). This location is slightly inside the pedestal top where gradients are considerably smaller than in the respective pedestals themselves, so that generally, they are not very different from the value at the top of the pedestal, and so, $(n_e^{\text{ped}}, T_e^{\text{ped}}) \sim (n_e^{95}, T_e^{95})$. We use this location instead of the top of the pedestal defined by the mtanh to facilitate the use of collisionality as explained below in Section 4.1. Indeed T_e^{95} varies dramatically in this set of experiments. In fact, within error bars, these pedestals cluster at opposite corners of the operational space - at high n_e^{95} and low T_e^{95} , and low n_e^{95} and high T_e^{95} . For the remainder of the paper, we distinguish the former using purple and the latter using green. Purple markers are also those at low P_{net} and high

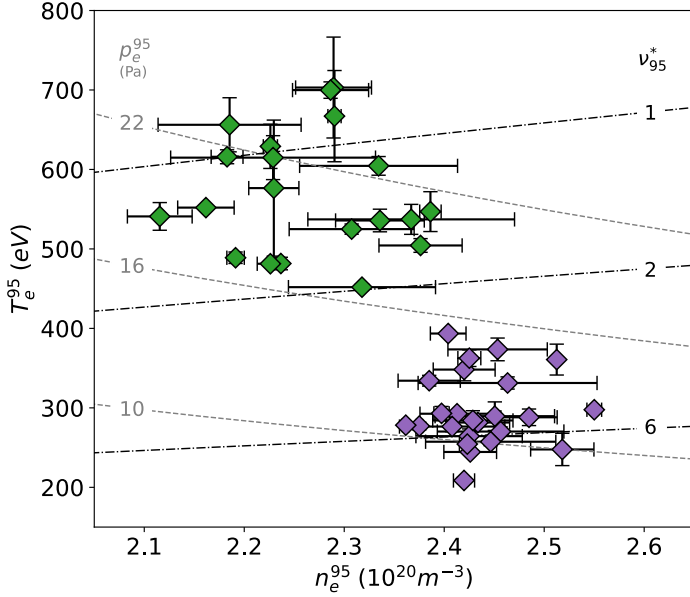


Figure 6: Pedestal top operational space in terms of (n_e, T_e) at $\psi_n = 0.95$. Purple diamonds are at high n_e and low T_e , while green diamonds are at low n_e and high T_e . Isobars (gray, dashed) and constant collisionality contours (black, dash-dotted) are included.

Γ_D , while green ones at higher P_{net} also maintain lower Γ_D . We make a more quantitative distinction between these in the next section.

4.1. Pressure and collisionality

Figure 6 includes both isobars in gray, dashed curves and constant collisionality contours (CCC) in and black, dash-dotted curves. The curves are both calculated at $\psi_n = 0.95$. The isobars are calculated using $p_e = n_e T_e$ and the CCCs are calculated using $\nu_{95}^* = \frac{q_{95} R_0 \nu_{ei}}{\epsilon^{3/2} v_{th,e}}$, where q_{95} is the safety factor at $\psi_n = 0.95$, R_0 is the plasma major radius, ν_{ei} is the electron-ion collision frequency, ϵ is the inverse aspect ratio, and $v_{th,e}$ is the electron thermal velocity. $\nu_{e,i}$ depends on Z_{eff} , the effective charge of the plasma, which is a difficult quantity to measure on C-Mod. Since these plasmas did not have extrinsic impurity seeding, Z_{eff} is taken to be 1.4, a common assumption for relatively pure plasmas on C-Mod. Since all of these plasmas are at similar B_t and I_P , there is little variation in q_{95} , so we calculate the CCCs from its average, $\langle q_{95} \rangle = 4.7$. From Figure 6, it is apparent that these pedestals range substantially both in p_e^{95} and ν_{95}^* . Pedestals with low D_{eff} can reach up pressures up to $p_e^{95} = 26.5$ kPa, more than twice that of pedestals with high D_{eff} . Conversely, transport-ridden pedestals at low p_e^{95} can reach collisionalities close to $\nu_{95}^* = 10$. Despite rather continuous changes in heat and particle sources as seen in Figure 2, there appears to be a quite clear separation in ν_{95}^* . Green points are those at $\nu_{95}^* < 2$ and the purple points are those at $\nu_{95}^* > 2$.

Plotting p_e^{95} against ν_{95}^* as in the top left panel of Figure 7 yields a relatively scatter-free correlation. Clearly, collisionality imposes rather strict regulation on the pedestal

pressure, with $p_e^{95} \sim (\nu_{95}^*)^{-0.5}$ across both groups of data. In fact, it seems that collisionality not only affects the attainable p_e^{ped} , but *also* the pressure pedestal gradient, ∇p^{ped} . Previous pedestal analysis on C-Mod has observed that the dimensionless pressure gradient is linked to the pedestal collisionality [18]. The right panel of Figure 7 supports this, showing the normalized pressure gradient, α_{MHD} , plotted against ν_{95}^* , where $\alpha_{\text{MHD}} = \frac{2\mu_0 q_{95}^2 R_0}{B_t^2} \nabla p$. We use the maximum ∇p in the edge, not strictly co-located with the center of the n_e pedestal. Since T_i measurements were not available for these discharges, we take $p_i = p_e$ and hence, set $\nabla p = 2\nabla p_e$. Furthermore, the expression used here is for a circular cross section and does not account for geometric corrections. Since the plasma shape is constant in all discharges shown here and the values of α_{MHD} reported are not meant to make direct contact with a stability analysis but rather motivate the governing physics, we opt for this simplified version. Note that most parameters in α_{MHD} are relatively constant across these discharges, with the exception of ∇p_e . In other words, changes in α_{MHD} are primarily changes in ∇p_e in this dataset.

As with p_e , ∇p_e is very tightly regulated by collisionality, decreasing even more strongly with ν_{95}^* . At low ν_{95}^* , $\alpha_{\text{MHD}} \sim (\nu_{95}^*)^{-0.9}$. At high ν_{95}^* , the dependence is slightly weaker, with $\alpha_{\text{MHD}} \sim (\nu_{95}^*)^{-0.7}$. It may be that as ν_{95}^* increases further, α_{MHD} reaches some minimum value required to sustain an H-mode. When comparing against collisionality at the separatrix, ν_{sep}^* , both p_e^{95} and α_{MHD} trend more strongly across the range in ν_{sep}^* , with $p_e^{95} \sim (\nu_{\text{sep}}^*)^{-0.8}$ and $\alpha_{\text{MHD}} \sim (\nu_{\text{sep}}^*)^{-1.3}$. They exhibit greater scatter, however, perhaps as a result of the radial separation in the parameters on the ordinate and abscissa.

Weakening of ∇p_e can be a symptom of differences in the position of the n_e pedestal relative to the T_e pedestal. Since ∇p_e consists of both ∇n_e and ∇T_e , its value is strongly related to the position of each gradient. Misalignment in the positions of maximum gradient strongly impact α_{MHD} . The relative shift of the two profiles has been previously observed and is thought to be a fueling effect, where the peak of the ionization moves radially outward, increasing density and locally cooling the plasma [18, 49, 50, 51, 52, 53]. Of course, ∇p_e can also decrease if either of its constituent gradients decreases. In this dataset, discharges at low ν^* (green) have a relative density and temperature shift, $\Delta R_{n-T}^{\text{ped}} = \Delta R_{n\text{-ped}} - R_{T\text{-ped}} = 1.4$ mm, whereas those at high ν^* (purple) have a relative shift $\Delta R_{n-T}^{\text{ped}} = 2.0$ mm. On the other hand, low ν^* discharges have on average, a maximum $\nabla T_e \approx 123$ keV m $^{-1}$, whereas high ν^* discharges only have a maximum $\nabla T_e \approx 32$ keV m $^{-1}$ on average. When multiplied by $\frac{R}{T_e^{\text{ped}}}$ as in [54], giving an estimate of the T_e gradient scale length, L_{T_e} normalized by machine major radius, R , the discharges at low ν^* have an average $\frac{R}{L_{T_e}} \approx 162$, while those at high ν^* have an average $\frac{R}{L_{T_e}} \approx 76$, less than half of those at low ν^* . While the gradients are computed at a different radial location than in [54], it is informative to note that multi-machine scalings may diverge in these very high ν^* pedestals. Indeed, it appears that as ν_{95}^* increases,

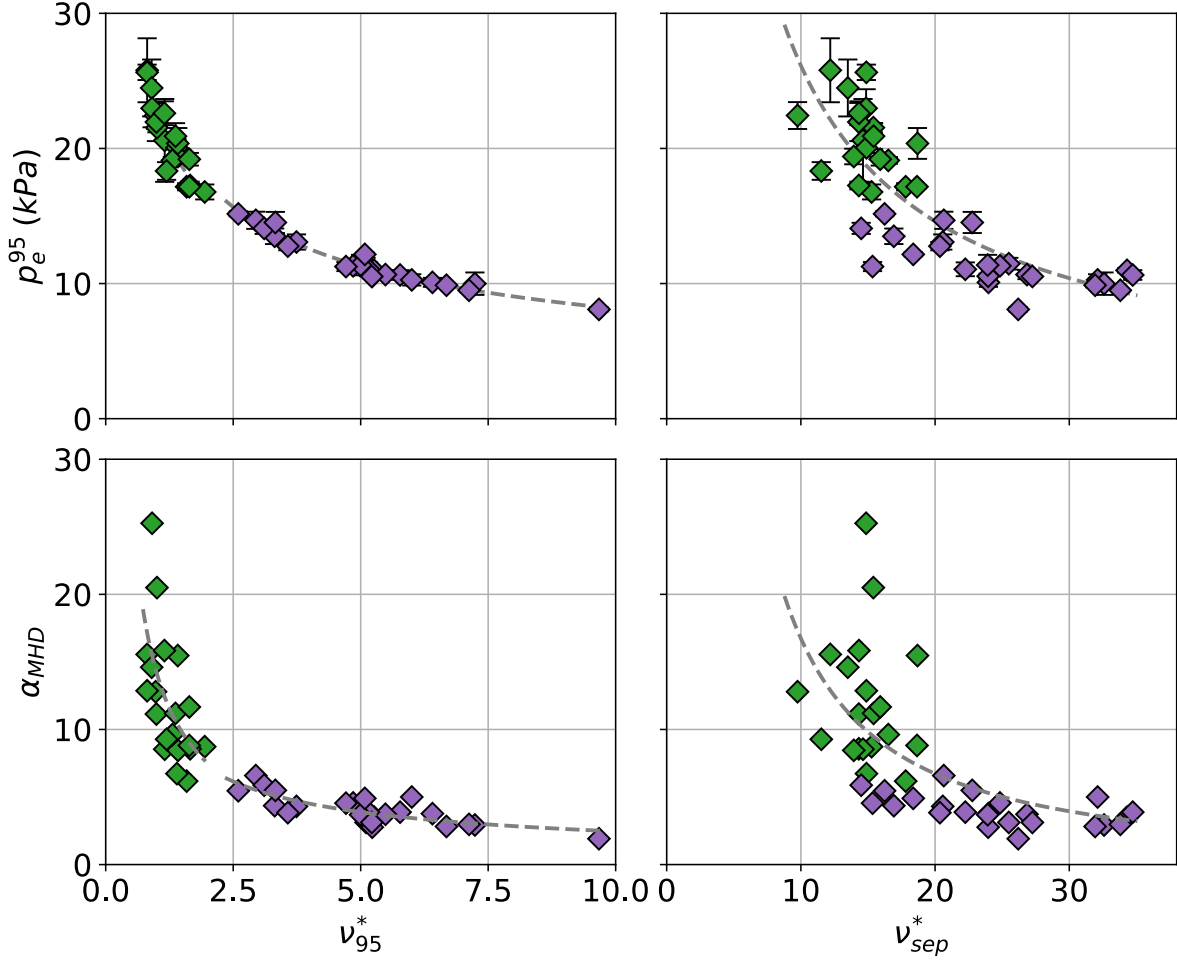


Figure 7: Pressure at $\psi_n = 0.95$ (top) and maximum normalized pressure gradient (bottom) plotted against collisionality at $\psi_n = 0.95$ (left) and at the separatrix (right). In both plots at left, there is a clear dependence of p_e^{95} and α_{MHD} on ν_{95}^* , whereby higher ν_{95}^* inhibits large pedestal pressure or pressure gradient. Plotting against ν_{sep}^* shows similar dependence, but with a less abrupt transition in ν^* . Shown also are power law fits, to both high and low ν_{95}^* points separately for the plots on the left, and across the full range of ν_{sep}^* for those on the right. For the plot on the top left, both high and low ν^* discharges trend in the same way, with $p_e^{95} \sim (\nu_{95}^*)^{-0.5}$. For the plot on the bottom, α_{MHD} decreases more strongly at low ν^* and more weakly at high ν^* . Their trends for low and high ν^* are $\alpha_{\text{MHD}} \sim (\nu_{95}^*)^{-0.9}$ and $\alpha_{\text{MHD}} \sim (\nu_{95}^*)^{-0.7}$, respectively. When regressing against ν_{sep}^* , as in the plots on the right, a stronger dependence is found for both p_e^{95} and α_{MHD} , with $p_e^{95} \sim (\nu_{\text{sep}}^*)^{-0.8}$ and $\alpha_{\text{MHD}} \sim (\nu_{\text{sep}}^*)^{-1.3}$.

it is primarily the ∇T_e weakening that is responsible for the weakening of α_{MHD} and a threat to fusion performance, reliant on a strong ∇p .

4.2. Transport variation with pedestal parameters

Simultaneous changes in p_e , ∇p_e and ν^* make it challenging to discern causality. Regardless, it is clear from Section 3 that there are large changes to D_{eff} , which appear to affect pedestal character substantially, most notably by limiting n_e . Observing that the discharges colored in purple are also more collisional, it is natural to question whether pedestal collisionality may be responsible for driving this increased transport. To test this hypothesis, the left panel of Figure 8 shows how D_{eff} at mid-pedestal, $D_{\text{eff}}^{\text{mid}}$, varies with ν_{95}^* . Not surprisingly, there is an increase in $D_{\text{eff}}^{\text{mid}}$ as ν_{95}^* increases. Regardless, the increase in D_{eff} with ν_{95}^* is evident only for $\nu_{95}^* > 2$. The right panel of Figure 8 shows the same metric for transport on the ordinate, but now as a function of ν^*

calculated at the separatrix. At the separatrix, ν^* can be almost an order of magnitude higher than at the pedestal top. Given the large gradients in the H-mode pedestal this variation is not surprising. Plotting transport against ν_{sep}^* yields a smoother correlation between transport and collisionality, implying that the separatrix conditions may more strongly influence pedestal gradients in these EDA H-modes than those at the pedestal top.

4.3. Influence of separatrix condition on pedestal gradients

That the separatrix encodes information about gradients and confinement inside the separatrix is not a novel concept. It has been previously observed on ohmic discharges on C-Mod that conditions around the separatrix strongly influence pressure gradients and the subsequent accumulation of plasma pressure inside of the separatrix [20]. Using a similar framework of electromagnetic fluid drift turbulence, it has been shown on ASDEX Upgrade

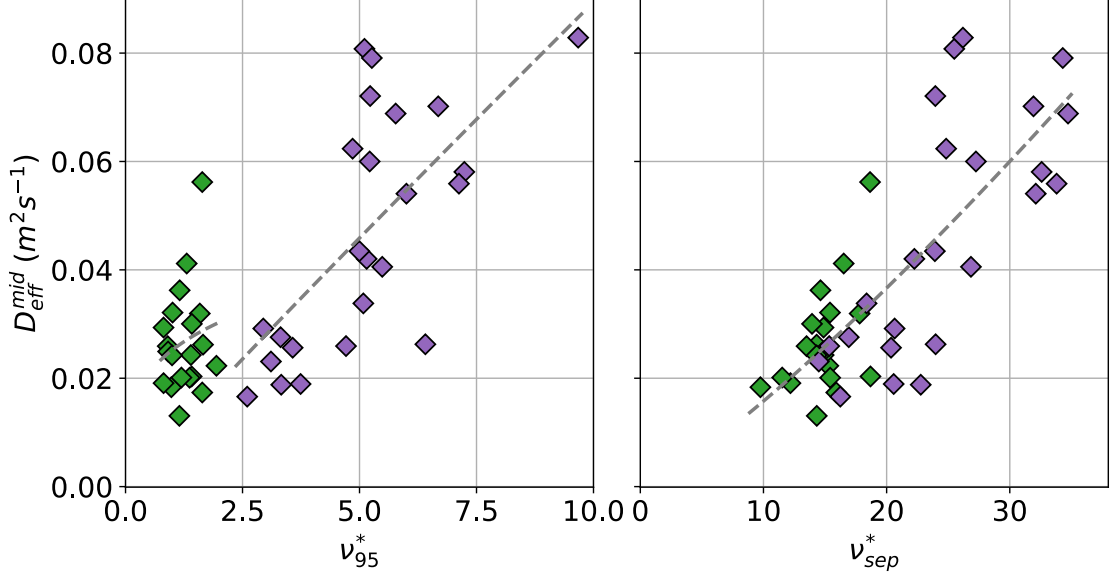


Figure 8: Inferred D_{eff} at mid-pedestal plotted against collisionality at $\psi_n = 0.95$ (left) and the separatrix (right), both using q_{95} . Dashed lines represent power law fits to green and purple discharges independently. There is a clear separation in collisionality at the top of the pedestal. For low values of ν^* , there is an unconvincing trend of $D_{\text{eff}}^{\text{mid}} \sim (\nu_{95}^*)^{0.3}$. At high ν_{95}^* , the trend is clearer - $D_{\text{eff}}^{\text{mid}} \sim (\nu_{95}^*)^{1.0}$. When plotting against ν^* at the separatrix, the separation on the abscissa disappears and both sets of points see even stronger trends in the mid-pedestal particle transport of $D_{\text{eff}}^{\text{mid}} \sim (\nu_{\text{sep}}^*)^{1.2}$.

(AUG) that the (n_e, T_e) operational space at the separatrix may strongly influence the overall plasma confinement regime as well as proximity to density limit-induced plasma disruption [55, 56]. These works apply interchange-drift-Alfvén turbulence theory, identifying α_t as an important turbulence control parameter. The full expression for α_t can be found in Equation 10 of [57], but for these C-Mod plasmas with $Z_{\text{eff}} = 1.4$, it can be approximated by Equation 7.

$$\alpha_t = 2.98 \times 10^{-18} R_{\text{geo}} \hat{q}_{\text{cyl}}^2 \frac{n_e}{T_e^2} Z_{\text{eff}} \quad (7)$$

Here, R_{geo} is the geometric major radius, taken to be equal to the device major radius, R_0 , and \hat{q}_{cyl} is the cylindrical safety factor, calculated according to $\hat{q}_{\text{cyl}} = \frac{B_t}{B_p} \times \frac{\hat{\kappa}}{R_{\text{geo}}/a_{\text{geo}}}$, where a_{geo} is the geometric minor radius, taken equal to the device minor radius, and $\hat{\kappa}$ is the effective elongation, defined in [55] in terms of triangularity and geometric elongation, which in this work is taken as the elongation calculated by EFIT.

It is observed that large values of α_t can widen the pressure gradient scale length (λ_p) at the separatrix [57]. Note that this parameter has the same form as the previously plotted ν^* , but includes a quadratic rather than linear dependence on the safety factor, q . The importance of this additional factor on q was noticed earlier as well in the work on C-Mod [20]. There, it was shown that λ_p organized better across different values of q_{95} when including this additional factor of q . In the current work, the plasmas are at similar q_{95} , so little re-organization of data occurs when plotting against α_t instead of ν^* . Doing so, however, points to a possible physical explanation. Figure 9 indicates that the transition between the high pressure and low pressure pedestals corresponds to values approaching and exceeding

unity, the range in which resistive ballooning mode (RBM) turbulence is thought to exert strong influence over drift-wave (DW) in [55]. As the separatrix gets denser and colder and α_t approaches unity, RBMs may begin to drive particle transport, substantially increasing D_{eff} .

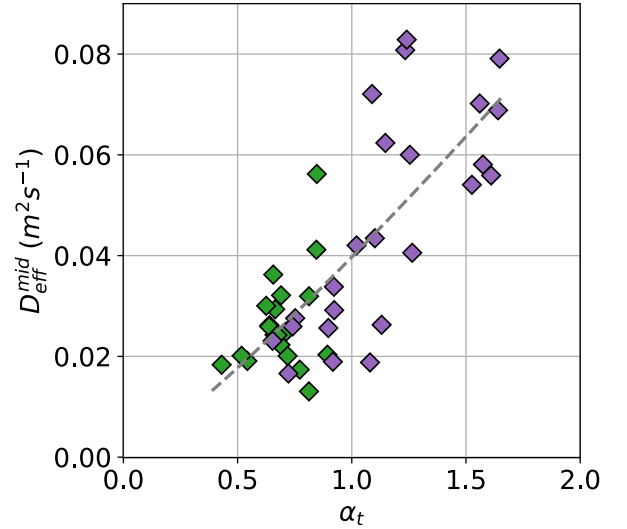


Figure 9: Inferred D_{eff} at mid-pedestal plotted now against α_t , a collisionality-like turbulence control parameter in interchange-DALF theory. It is suggested that when α_t reaches unity, edge turbulence transitions from DALF to interchange. The trend across both regimes is the same as with ν_{sep}^* , with $D_{\text{eff}}^{\text{mid}} \sim \alpha_t^{1.2}$.

5. Neutral modeling and interpretive transport solutions with SOLPS-ITER

The technique outlined in Section 2 is powerful in that it can be employed across an entire database of shots with high quality Ly_α and ETS data. These are 1D measurements, however, so any conclusions about transport hinge on assumptions about the poloidal distribution of neutrals. If Γ_D estimated at the outer midplane (OMP), Γ_D^{OMP} , is significantly different its flux-surface averaged value, Γ_D^{FSA} , the experimentally inferred D_{eff} may not be wholly indicative of transport in the pedestal across its poloidal extent. Experimental estimates of D_{eff} made here assume that variation in the poloidal fueling profiles between shots is small and that generally, this peaks at or near the poloidal location observed by the Ly_α camera (here, the OMP). Furthermore, without some interpretive power balance analysis using a transport code, we can only investigate the particle transport and know little about changes to the electron or ion thermal transport. To gain insight into thermal transport, compare with our inferences of particle transport from 1D analysis, and learn about poloidal distribution of neutrals, we choose certain discharges from these experiments to simulate with SOLPS-ITER, a code suite used extensively for edge modeling of plasma and neutrals. SOLPS-ITER couples a 2D multi-fluid plasma transport code, B2.5, with a 3D kinetic Monte Carlo neutral transport solver, EIRENE [58]. In the current study, we focus primarily on the OMP and constrain the plasma and neutral models there. The simulations are performed for only deuterium, D, ion species.

5.1. Plasma constraints

5.1.1. Boundary conditions For the plasma solution, we reproduce n_e and T_e from the top of the pedestal to the near-SOL using profile fits to the ETS measurements. At the core boundary, we prescribe input power and particle fluxes. We take P_{net} from experiment and assume energy equipartition, providing $\frac{1}{2}P_{\text{net}}$ to each the electron and the ion populations. While the exact partition of energy in the edge can vary in different plasmas, the assumption of equal heat fluxes falls within a range of values estimated from TRANSP runs of a number of C-Mod plasmas [59]. Applying P_{net} at the innermost flux surface of the B2.5 plasma grid rather than at the separatrix assumes negligible radiated power in the plasma annulus about 1 cm thick between this flux surface and the separatrix. For the particle flux, we set $\Gamma = 0$. Alcator C-Mod had no core particle source, neither via neutral beam injection (NBI), nor pellet-fueling. Any non-zero Γ at the innermost boundary of the B2.5 grid comes entirely from neutrals recycled at its walls, assumed to be negligible. This is checked a posteriori to be a valid assumption, as shown below in Section 5.2.

Because of the small $\Delta R_{\text{sep}} \approx 5$ mm, a disconnected DN grid is used, yielding four targets in the simulation domain. At each of these, sheath BCs are used, set via the usual modified Bohm criterion. For the SOL and private flux region (PFR), BCs are set to the “leakage”

type, instead of the more conventional “decay length” type. The choice for these BCs is important for reproducing the details of the neutral profiles and are outlined in Section 5.2. Finally, motivated by a study for the importance of using heat flux limiters to match simulations to experimental C-Mod divertor temperature measurements [60], flux limiters for the thermal parallel transport are included in the simulations, using a value of 0.15 for both ions and electrons.

5.1.2. Transport coefficients For particle transport, we assume purely diffusive transport, specifying the particle density diffusion coefficient, D_n . For energy, we use thermal diffusivity coefficients, χ_e for the electrons, and χ_i for the ions. To reproduce the steep gradients in these H-mode edges, it is necessary to apply a transport well by using a radially-varying profile in all three channels. We ignore poloidal variation of transport coefficients in the core and specify transport profiles to reproduce n_e and T_e measurements from ETS, at the OMP. This is likely a source of error, as previous work on C-Mod has shown that ballooning-like transport drives larger plasma fluxes to the outboard rather than inboard side of the core [43]. As a result, the D_{eff} reported in this work may represent an underestimation of the transport on the LFS and an overestimation on the HFS. We further assume negligible poloidal variation in radial transport along open field lines in the SOL, such that the same transport coefficient profile at the midplane SOL is used at the divertor targets. Finally, we use flat transport coefficients in the PFR: $D_n = 5 \times 10^{-2} \text{ m}^2 \text{ s}^{-1}$ and $\chi_e = \chi_i = 7 \times 10^{-1} \text{ m}^2 \text{ s}^{-1}$.

To determine transport profiles for the plasma in the main chamber and SOL, we employ an iterative approach used to reproduce TS profiles on NSTX and DIII-D [61, 62]. The approach uses a set of transport coefficient profiles at iteration j to evaluate a new set of profiles at iteration $j + 1$ by using the experimental gradients, according to the following,

$$D_n^{\text{SOLPS},j+1} = -\frac{\Gamma^{\text{SOLPS},j}}{\nabla n^{\text{exp}}} \quad (8)$$

$$\chi_{e,i}^{\text{SOLPS},j+1} = -\frac{q_{e,i}^{\text{SOLPS},j} - \frac{5}{2}\Gamma^{\text{SOLPS},j}T_{e,i}^{\text{SOLPS},j}}{n^{\text{exp}}\nabla T_{e,i}^{\text{exp}}} \quad (9)$$

where $q_{e,i}$ is either the electron or ion heat flux. Equation 9 is solved for electrons and ions separately. Since ion temperature, T_i , measurements are unavailable for these cases, we assume $T_e = T_i$, and set $\nabla T_i^{\text{exp}} = \nabla T_e^{\text{exp}}$ in the calculation of χ_i . Earlier work comparing T_i to T_e showed that the temperature ratio, $\tau_i = T_i/T_e$, was not far from unity at the pedestal, but could be as high as six at the separatrix and in the SOL [60]. τ_i was found to be most clearly dependent on divertor collisionality - the more collisional the divertor, the more equilibrated T_i and T_e . Given that the EDA plasmas in the current study were very collisional, $\tau_i = 1$, while likely an under-estimation, may not be wholly inaccurate, at least through the pedestal. Recent simulations of DIII-D have tested various approaches

Shot	P_{net} (MW)	T_e^{95} (eV)	n_e^{95} (10^{20} m^{-3})	n_0^{sep} (10^{16} m^{-3})	ν_{sep}^*
1070821003	1.4	240	2.4	3.7	28
1070821004	2.0	280	2.5	3.0	24
1070821009	2.9	480	2.2	2.6	21
1070821008	3.4	700	2.3	2.5	13

Table 2: Relevant parameters pertaining to the four selected discharges to be simulated using SOLPS-ITER. As before, the discharges at low P_{net} have high n_e , low T_e , and high n_0 . The opposite is true for the discharges at high P_{net} .

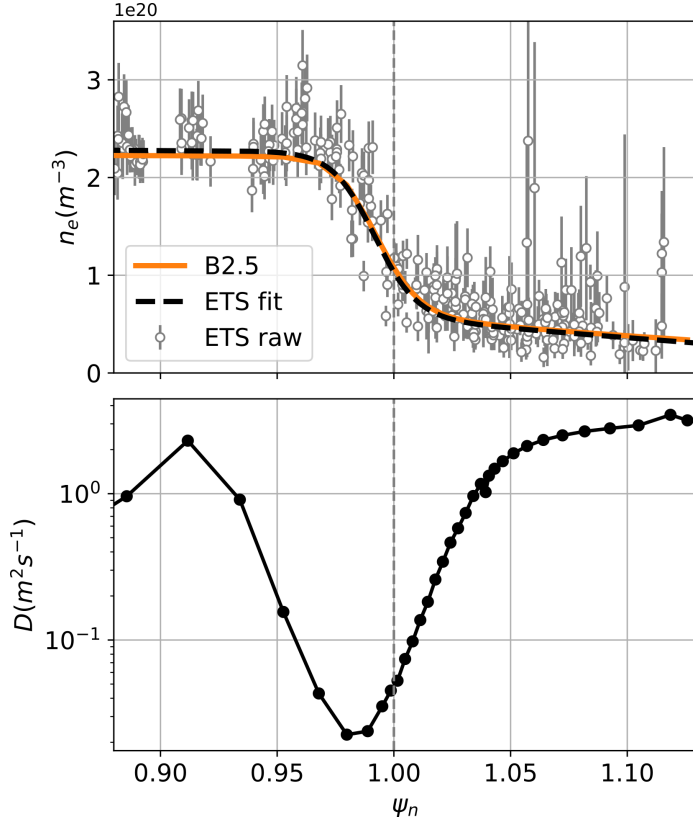


Figure 10: Electron density (top) and particle diffusion coefficient (bottom) from a converged SOLPS simulation. The top plot shows the experimental ETS data points and their errorbars in open, gray circles, as well as the best mtanh fit (dashed black line) computed from the least-squares minimization procedure outlined in Section 2.3. The orange line shows the resulting n_e after a set of iterations to determine the $D(\psi_n)$ profile, plotted below, that would best reproduce the experimental $n_e(\psi_n)$, while simultaneously matching $n_0(\psi_n)$.

to setting the T_i temperature. They show sensitivity of outputs, namely increased neutral pressure in the PFR at higher values of T_i upstream. This motivates more detailed study of the sensitivity of upstream $n_0(\psi_n)$, specifically in the pedestal, to choice of T_i [62].

Figure 10 shows an example of experimental ETS data and the corresponding mtanh fit. Plotted also is the simulated n_e profile as well as the corresponding D_n profile used to match the experimental ∇n_e from the mtanh fit. Using this iterative transport solving scheme, between 25 – 35% of input power exits the grid radially across the outer grid boundary, presumably hitting the first wall and

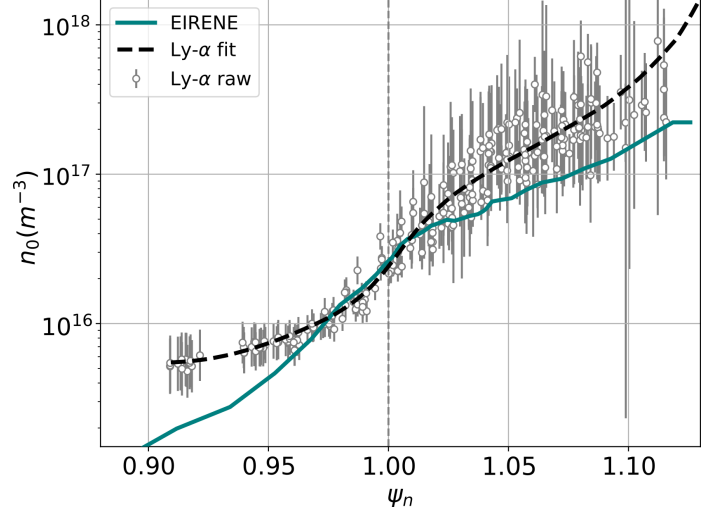


Figure 11: The neutral density profile used to constrain the EIRENE solution, in log scale. In open, gray circles are the points, along with the error bars, corresponding to the measured n_e and T_e from ETS, onto which $\epsilon_{\text{Ly}\alpha}$ is interpolated to experimentally infer n_0 . The dashed black line represents the n_0 computed from the experimental profile fits. In turquoise is the simulated profile computed by EIRENE and interpolated onto the B2.5 plasma grid. This profile has been tuned using the procedure in Section 5.2 to get as best a visual match in the pedestal region as possible.

not arriving at the divertor. Furthermore, for simplicity, the code is run without including fluid drifts or currents.

5.2. Neutrals constraints

A consequence of Equation 8 is that without a constraint for Γ^{SOLPS} , any number of values of D_n can reproduce the requisite ∇n^{exp} . In other words, n_e on its own is insufficient to constrain Γ^{SOLPS} and thus, D_n . As shown in Section 2, knowing n_0 or equivalently S_{ion} fixes Γ_D , which does constrain the EIRENE calculation. Therefore, only if we can simultaneously match n_e , T_e , and n_0 at the OMP can we confidently make a conclusion about D_n , as well as χ_e [27], at least in a poloidally-averaged sense.

Recent work on Alcator C-Mod has helped validate the n_0 calculation in EIRENE using the same LYMID camera [27] across confinement modes. As mentioned in Section 5.1.1, rather than specifying a decay length given by n_e and D_n at the outermost grid cell, we use leakage BCs. These insist that the particle flux returning from the vessel walls be proportional to the local sound speed, c_s ,

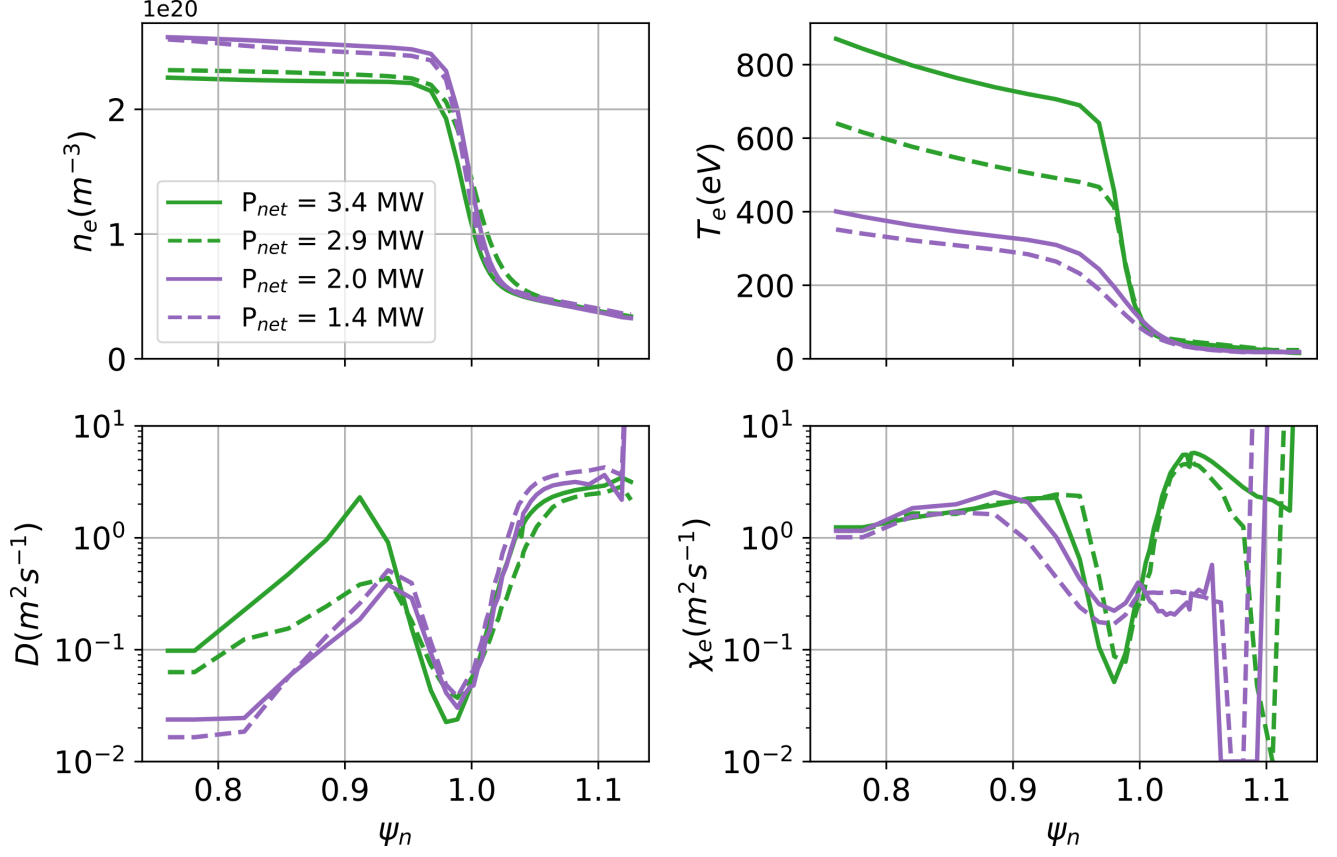


Figure 12: Pedestal plasma solutions (top) and transport coefficient profiles (bottom) for the four simulated discharges tabulated in Table 2. Quantities are shown for the particle transport channel (left) and for the electron thermal transport channel (right). n_e and D profiles are largely similar in shape. T_e and χ_e profiles are not, varying significantly in height and in width. In the absence of T_i measurements, χ_i is used simply to enforce $T_e = T_i$ and is not shown, as physical significance is uncertain.

and n , i.e. $\Gamma \sim \sqrt{\frac{T_e + T_i}{m_i}} n$. The current work finds that the proportionality constant for the particle channel, the particle leakage coefficient, α_n , sets the magnitude of Γ (and by consequence, n_0). This BC is thus used to shift n_0 up and down in magnitude, attempting primarily to match the magnitude of n_0 in the pedestal. While α_n changes the magnitude of n_0 it keeps the neutral gradient scale length, L_{n_0} , in the pedestal, $L_{n_0}^{\text{ped}}$, i.e. the shape of the neutral density profile, relatively fixed. Previous studies of neutral penetration shows that L_{n_0} depends strongly on n_e [15]. Since we are seeking a match to n_e , we must also match L_{n_0} , and we instead mobilize the thermal leakage coefficients for electrons, α_{T_e} , and ions, α_{T_i} , to tune $L_{n_0}^{\text{ped}}$. These essentially modify $q_{e,i}$, which indirectly affects Γ_D by modifying the shape of n_0 . The coefficients $\{\alpha_n, \alpha_{T_e}, \alpha_{T_i}\}$ thus become the toolkit needed to match both the magnitude and slope of n_0 across the pedestal, given a particular B2.5 solution. Updating the EIRENE solution, however, also affects B2.5 by modifying the sources for the plasma transport equations. This essentially adds an outer loop to the iterative process described in Section 5.1.2. Figure 11 shows an example of the n_0 profile, calculated by EIRENE and interpolated onto the B2.5 grid, which results from this tuning process and which corresponds to the case shown in Figure 10.

For these discharges, the simulation domain is treated as an isolated system, with no injection or removal of

particles. Since Alcator C-Mod had molybdenum walls which did not readily absorb deuterium, we set the albedo to unity at all vessel walls, including targets. As mentioned in Section 5.1.1 we impose $\Gamma = 0$ at the core boundary. Recalling that these H-modes were not actively puffed (see Section 2), we also do not inject gas into the simulation domain via gas puffing. Particle balance is therefore achieved in these simulations simply by manipulating the initial particle inventory.

5.3. Transition in particle and thermal transport

Given the computational cost of these simulations, we select four discharges from the power scan to model, covering a range in P_{net} and ν^* . Two of these are below the critical P_{net} and two are above. Key parameters of the four simulated discharges are listed in Table 2. Figure 12 shows simulated n_e , T_e , D_n and χ_e profiles across the pedestal and into the SOL for the four simulated discharges. The n_e and T_e profiles shown here all closely match the fitted experimental profiles, within fit error bars. As expected, the high P_{net} discharges have prominent T_e pedestals and slightly lower n_e pedestals. As P_{net} drops, T_e^{ped} plummets and n_e^{ped} grows to the saturated level seen earlier, in Figure 4. At this scale, it is hard to discern variation in separatrix conditions. At the pedestal top, however, it is evident that the green curves are

at considerably lower ν^* than the purple curves, especially given the T_e^{-2} dependence in ν^* .

The bottom panels of Figure 12 show the transport profiles found to reproduce n_e, T_e and n_0 . In the pedestal, $D_n(\psi_n)$ shifts down and slightly radially inwards only at the highest value of P_{net} . There are no drastic changes to the structure of the profile in the steep-gradient region of the pedestal. This is not surprising given the apparent similarity in shape of the n_e profiles and the small variation in profile gradients. χ_e , on the other hand, clearly changes both in magnitude and in profile structure across the P_{net} scan. Indeed, the rise in transport observed in the particle channel is even larger in the electron thermal channel. The purple curves have much higher χ_e across the steep gradient region than the green curves. They also appear to shift slightly radially inward, in the opposite direction of D_n at low P_{net} . It follows then that the relative shift between n_e and T_e and weakening of α_{MHD} mentioned in Section 4 could also be explained by the spatial decoupling of the particle and electron thermal transport shear layers in low P_{net} plasmas. More notable, however, is the significant widening of $\chi_e(\psi_n)$ as P_{net} drops. The T_e pedestals at low P_{net} , shown in the top right panel, are considerably wider than those at high P_{net} . At the separatrix, $D \sim 6 \times 10^{-2} \text{ m}^2\text{s}^{-1}$ and $\chi_e \sim 3 \times 10^{-1} \text{ m}^2\text{s}^{-1}$ for all values of P_{net} . This change in χ_e best explains the weakening of the ∇T_e observed in Section 4.

In Figure 13, we plot the simulated D_n and χ_e onto the experimentally inferred D_{eff} , as a function of ν_{sep}^* . Indeed the simulated D_{eff} from SOLPS fall within the scatter of the experimental data, trending upwards with collisionality. This acts as a confirmation that the use of 1D analysis of plasma and neutral profiles as described in Section 2 yields a value for D_{eff} consistent with the poloidally-averaged one used in the SOLPS simulations. Of course, as different machines may have different poloidal neutral distributions, this confirmation is not in general the case across machines. Figure 13 shows that it is actually χ_e that undergoes the most dramatic transition at a critical collisionality, $\nu_{\text{sep},\text{crit}}^* \approx 22$. Interestingly enough, at $\nu_{\text{sep}}^* < \nu_{\text{sep},\text{crit}}^*$, $D_n \sim \chi_e$. At $\nu_{\text{sep}}^* > \nu_{\text{sep},\text{crit}}^*$, however, $D_n \ll \chi_e$. Recent computational work using pedestal gyrokinetics has indicated that the ratio of diffusivities in the pedestal in different transport channels may be indicative of different transport drives [63]. Indeed this may be consistent with the earlier assertion of transition in the character of turbulence from Figure 9.

6. Discussion

As mentioned in Section 3, pedestal stiffness and critical gradient-like behavior in the edge of Alcator C-Mod is not a new finding. Given C-Mod's proximity in parameter space to next-generation devices [64, 65, 66], it is imperative to develop improved understanding for the conditions under which this phenomenon occurs. This paper proposes collisionally-driven transport as the mechanism by which a pedestal at its natural density responds to increased neutral flux and regulates its density gradient. As shown in Figure 4, as $S_{\text{ion}}^{\text{sep}}$ increases, so does n_e^{sep} . Higher $S_{\text{ion}}^{\text{sep}}$ corresponds

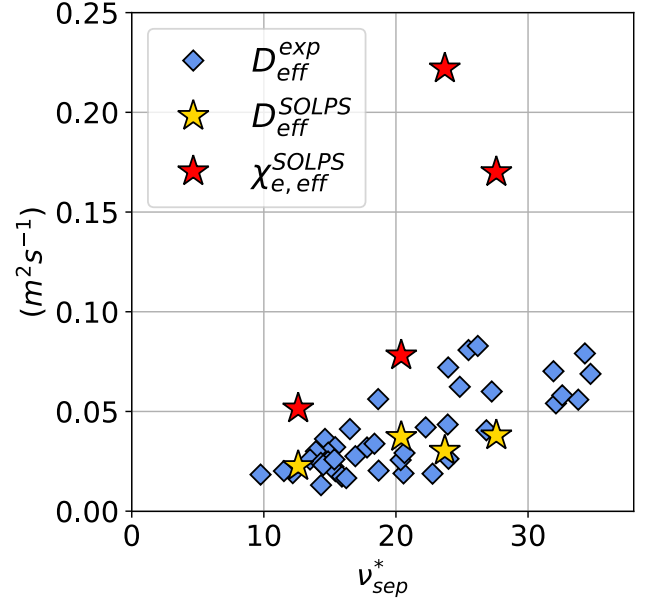


Figure 13: Transport coefficients, inferred experimentally (diamonds) or computationally (stars) against separatrix collisionality. The blue diamonds are the experimentally inferred particle transport coefficients. The yellow stars are the same coefficients, but determined computationally using Equation 8 iteratively. The red stars are the electron thermal transport coefficients determined via the simulation, using the electron component of Equation 9. D_{eff} coefficients are extracted at mid- n_e pedestal, while χ_e is extracted at mid- T_e pedestal. $D_{\text{eff}}^{\text{SOLPS}}$ fall within the scatter of $D_{\text{eff}}^{\text{exp}}$, while χ_e^{SOLPS} is larger at high ν_{sep}^* but closer in magnitude at low ν_{sep}^* .

to an increase in n_0^{sep} as well, which presumably increases plasma thermal sinks, dropping T_e^{sep} . The concomitant drop in T_e^{sep} ultimately drives pedestals that are dense with neutrals to higher collisionalities. Figures 8 and 9 show that as the collisionality at the separatrix increases, so does α_t , as well as D_{eff} , likely as a result of a change in the nature of the transport. Figure 5 shows that when the gradient reaches a certain value, increased fueling increases transport, and at large enough values, the gradient begins to shrink. This additional resistive transport mechanism necessitates the use of varying diffusive transport coefficients. Given that these plasmas are all in the EDA regime, it is natural to question whether pedestal regulation via separatrix collisionality is inherently a feature of this regime. It has been shown on Alcator C-Mod that in EDA H-modes, the density fluctuations characteristic of the quasi-coherent mode (QCM) may be linked to increased particle transport [67]. Analysis to evaluate possible links between the QCM and the type of transport described here are ongoing.

It is important to note that this work says little about how a pedestal might reach a critical gradient to begin with and what types of devices might be susceptible to reaching one. Two characteristics of Alcator C-Mod, both hinted at above, appear important. The first of these is a neutral effect, which affects particle transport via indirect modification of collisionality. Having operated at the highest of plasma densities, C-Mod is proposed

to be the device closest to the opaqueness predicted on both SPARC and ITER [15]. Inability to fuel inside the pedestal will push the ionization front radially outward, increasing collisionality at the separatrix or in the near SOL, thereby exacerbating the gradient regulation via resistive transport. This may very well occur at high densities in future machines. It is important to note that in terms of typical length scales, e.g. the poloidal gyroradius, the pedestal width, or the machine size, Alcator C-Mod is in a somewhat different parameter regime than future reactors. When considering dimensionless quantities, however, like opaqueness, or the gyroradius normalized to the minor radius, ρ^* , linked to both neoclassical and turbulent transport, this is not entirely the case. As for ν^* , the parameter identified in this work as responsible for enhanced pedestal transport, large radial variation in this value makes it difficult to make conclusions about reactor-relevance, as noted in Section 4.2.

The second effect is related to the poloidal distribution of neutrals on C-Mod. It existed in the so-called main chamber recycling regime [23], consistent with large radial particle fluxes observed at the OMP. Measurements from a gas puff imaging system as well as from a stochastic model imply that this is linked to large filaments called “blobs” propagating radially outward, depositing a large number of particles and heat to the main chamber walls [68]. In either case, large particle fluxes to the MC walls means high main chamber neutral density, setting up a plasma environment conducive to the rise of RBMs at or near the separatrix. While it is unclear if the cause of high MC fueling on C-Mod is its high density or rather the close-fitting wall, these features will also be present on next-generation devices, and MC recycling may continue to comprise a large fraction of the fueling dynamics.

That these C-Mod pedestals exhibit what appears to be a limit to gradient growth has a number of implications for new fusion devices. To realize sufficient fusion gain, reactors will require high core densities. These must also be compatible with robust pedestals for good confinement. This work shows that good confinement can be lost when P_{net} drops below a critical value, $P_{\text{net}}^{\text{crit}}$, even while remaining in H-mode. For the set of discharges analyzed, this critical value corresponds almost exactly to L-H power threshold, $P_{\text{th}}^{\text{L-H}}$, calculated from the Martin scaling [69]. This scaling has shown good agreement with power threshold experiments on C-Mod [70]. Across a wide range in I_p and \bar{n}_e , some deviations from the scaling exist at low and high I_p and \bar{n}_e , but for $I_p = 0.8$ MA, the data matches the scaling [71]. Since next-generation devices like SPARC and ITER, and later reactors, require high density and large plasma volumes, it is possible that they too will operate at P_{net} marginal to their corresponding $P_{\text{th}}^{\text{L-H}}$ [70, 71, 33].

It remains to be seen whether the observed transition to a collisional transport regime dictated by a collisional separatrix is inherently linked to $P_{\text{th}}^{\text{L-H}}$ in a quantitative way in general, or just by coincidence on C-Mod in this parameter range. Reactors, however, will likely require such a collisional separatrix with view of divertor handling [72], even if the pedestal is collisionless. Based on projections

for n_e^{sep} and T_e^{sep} found in [73, 74], ν_{sep}^* on SPARC may range anywhere from below 1 and up to 10. Operation at even higher n_e^{sep} might bring this value closer to values observed here. Additionally, the discharges analyzed here do not include seeded impurities. The lack of impurities allows for an easier estimate of Z_{eff} , which figures into ν^* , facilitating the analysis in this work. This may differ, however, from a reactor scenario where impurities may be used to access divertor detachment. We also note that this paper only includes analysis of H-modes that are not actively gas puffed, even with D gas. While intrinsic wall-recycling may sound attractive, it means density control is substantially more challenging, or at least that there is a strong (although perhaps indirect) link between P_{net} and plasma fueling.

7. Conclusions and future work

This work presents new analysis of archival data from Alcator C-Mod. It deploys the routinely used ETS together with the less-frequently analyzed LYMID data to study the role of fueling and transport on pedestals in a high density, opaque plasma edge. Using inferences of ionization rates, it is observed that n_e^{sep} is a strong function of S_{ion} , continuing to increase even at high S_{ion} . n_e^{ped} , on the other hand, stagnates, implying a saturated and even shrinking ∇n_e . Comparing this gradient with Γ_D shows a non-linear relationship, only explainable with varying D_{eff} , despite relatively fixed shape and q_{95} . Inspection of profiles inside the pedestal top shows that the phase space at this radial location is best categorized by p_e and ν^* . Highly collisional pedestals are also found to have lower values of α_{MHD} , consistent with worsening H-mode quality and thus, H_{98} . It is found that ν_{sep}^* is most influential in determining the large rise in D_{eff} across the pedestal and the subsequent flattening of the edge n_e profile. Initial analysis links this to changes in α_t , which mediates the transition between DW and RBM-dominated turbulence.

We supplement these experimental findings of changes to D_{eff} through modeling of selected discharges with the widely used edge code, SOLPS-ITER. High fidelity calculation of particle and heat sources, in addition to experimental 1D constraints, lends confidence to conclusions about how particle and heat transport must change to build up pedestal-gradients. Given the coupled nature of sources and transport demonstrated in this work, it recommends the development of models for the pedestal to include self-consistent accounting of both sources and transport. In particular, it allows for inference of χ_e (and χ_i to the degree that we trust the $\tau_i = 1$ assumption). Large growth in χ_e bolsters the claim that changes to the fundamental transport properties in these pedestals may be at play. Though not highlighted here, work has begun to understand how the poloidal distribution of neutrals may validate or limit the 1D inferences of D_{eff} from experiment. This, as well as understanding the contributions from different atomic processes to the neutral density in the pedestal, will be important steps in developing a model for the interplay between fueling and transport in the pedestal.

It has become evident that reactors will not be able to tolerate Type-I ELMs [33, 75, 76]. The non-ELMing behavior of the EDA H-mode, and other similarly non-ELMing modes, highlights the importance in understanding pedestal structure, and the mechanisms that determine it. While it is unclear if the EDA regime is achievable on reactors given that they will operate at high T_e^{ped} and thus, low ν_{ped}^* , some ELM-free solution is required. The analysis presented provides a useful experimental basis for how a pedestal may reach a transport limit before it is limited by less benign MHD events. It furthermore suggests that transport in the pedestal can be closely linked to the collisionality at the separatrix, even more so than at the pedestal top. Even if ν_{ped}^* were to remain low, as long as ν_{sep}^* remains high enough, transport regulation of pedestal gradients may persist, ensuring ELM-free operation. Given that reactors may operate at high n_e^{sep} for divertor survivability, the requisite ν_{sep}^* may not altogether be out of reach. As has been observed previously, high edge collisionality may also help widen near-SOL widths [77, 78], helping work towards an integrated core-edge exhaust solution.

References

- [1] ASDEX Team. The H-Mode of ASDEX. *Nuclear Fusion*, 29(11):1959–2040, November 1989.
- [2] M. Kotschenreuther, W. Dorland, M. A. Beer, and G. W. Hammett. Quantitative predictions of tokamak energy confinement from first-principles simulations with kinetic effects. *Physics of Plasmas*, 2(6):2381–2389, June 1995.
- [3] M. Greenwald, R.L. Boivin, F. Bombarda, P.T. Bonoli, C.L. Fiore, D. Garnier, J.A. Goetz, S.N. Golovato, M.A. Graf, R.S. Granetz, S. Horne, A. Hubbard, I.H. Hutchinson, J.H. Irby, B. LaBombard, B. Lipschultz, E.S. Marmar, M.J. May, G.M. McCracken, P. O’Shea, J.E. Rice, J. Schachter, J.A. Snipes, P.C. Stek, Y. Takase, J.L. Terry, Y. Wang, R. Watterson, B. Welch, and S.M. Wolfe. H mode confinement in Alcator C-Mod. *Nuclear Fusion*, 37(6):793–807, June 1997.
- [4] J.E. Kinsey, G.M. Staebler, J. Candy, R.E. Waltz, and R.V. Budny. ITER predictions using the GYRO verified and experimentally validated trapped gyro-Landau fluid transport model. *Nuclear Fusion*, 51(8):083001, August 2011.
- [5] L. Frassinetti, M.N.A. Beurskens, S. Saarelma, J.E. Boom, E. Delabie, J. Flanagan, M. Kempenaars, C. Giroud, P. Lomas, L. Meneses, C.S. Maggi, S. Menmuir, I. Nunes, F. Rimini, E. Stefanikova, H. Urano, and G. Verdoolaege. Global and pedestal confinement and pedestal structure in dimensionless collisionality scans of low-triangularity H-mode plasmas in JET-ILW. *Nuclear Fusion*, 57(1):016012, January 2017.
- [6] P. Rodriguez-Fernandez, N. T. Howard, M. J. Greenwald, A. J. Creely, J. W. Hughes, J. C. Wright, C. Holland, Y. Lin, F. Sciortino, and the SPARC team. Predictions of core plasma performance for the SPARC tokamak. *Journal of Plasma Physics*, 86(5):865860503, October 2020.
- [7] E.J. Doyle, W.A. Houlberg, Y. Kamada, V. Mukhovatov, T.H. Osborne, A. Polevoi, G. Bateman, J.W. Connor, J.G. Cordey, T. Fujita, X. Garbet, T.S. Hahm, L.D. Horton, A.E. Hubbard, F. Imbeaux, F. Jenko, J.E. Kinsey, Y. Kishimoto, J. Li, T.C. Luce, Y. Martin, M. Ossipenko, V. Parail, A. Peeters, T.L. Rhodes, J.E. Rice, C.M. Roach, V. Rozhansky, F. Ryter, G. Saibene, R. Sartori, A.C.C. Sips, J.A. Snipes, M. Sugihara, E.J. Synakowski, H. Takenaga, T. Takizuka, K. Thomsen, M.R. Wade, H.R. Wilson, ITPA Transport Physics Topical Group, ITPA Confinement Database And Model Group, and ITPA Pedestal And Edge Topical Group. Progress in the ITER physics basis chapter 2: Plasma confinement and transport. *Nuclear Fusion*, 47(6):S18–S127, June 2007.
- [8] P. Rodriguez-Fernandez, A.J. Creely, M.J. Greenwald, D. Brunner, S.B. Ballinger, C.P. Chrobak, D.T. Garnier, R. Granetz, Z.S. Hartwig, N.T. Howard, J.W. Hughes, J.H. Irby, V.A. Izzo, A.Q. Kuang, Y. Lin, E.S. Marmar, R.T. Mumgaard, C. Rea, M.L. Reinke, V. Riccardo, J.E. Rice, S.D. Scott, B.N. Sorbom, J.A. Stillerman, R. Sweeney, R.A. Tinguely, D.G. Whyte, J.C. Wright, and D.V. Yuryev. Overview of the SPARC physics basis towards the exploration of burning-plasma regimes in high-field, compact tokamaks. *Nuclear Fusion*, 62(4):042003, September 2022.
- [9] P.B. Snyder, N. Aiba, M. Beurskens, R.J. Groebner, L.D. Horton, A.E. Hubbard, J.W. Hughes, G.T.A. Huysmans, Y. Kamada, A. Kirk, C. Konz, A.W. Leonard, J. Lönroth, C.F. Maggi, R. Maingi, T.H. Osborne, N. Oyama, A. Pankin, S. Saarelma, G. Saibene, J.L. Terry, H. Urano, and H.R. Wilson. Pedestal stability comparison and ITER pedestal prediction. *Nuclear Fusion*, 49(8):085035, August 2009.
- [10] R.J. Groebner, P.B. Snyder, T.H. Osborne, A.W. Leonard, T.L. Rhodes, L. Zeng, E.A. Unterberg, Z. Yan, G.R. McKee, C.J. Lasnier, J.A. Boedo, and J.G. Watkins. Limits to the H-mode pedestal pressure gradient in DIII-D. *Nuclear Fusion*, 50(6):064002, June 2010.
- [11] J.R. Walk, P.B. Snyder, J.W. Hughes, J.L. Terry, A.E. Hubbard, and P.E. Phillips. Characterization of the pedestal in Alcator C-Mod ELMing H-modes and comparison with the EPED model. *Nuclear Fusion*, 52(6):063011, June 2012.
- [12] P.B. Snyder, J.W. Hughes, T.H. Osborne, C. Paz-Soldan, W.M. Solomon, M. Knolker, D. Eldon, T. Evans, T. Golfinopoulos, B.A. Grierson, R.J. Groebner, A.E. Hubbard, E. Kolemen, B. LaBombard, F.M. Laggner, O. Meneghini, S. Mordijck, T. Petrie, S. Scott, H.Q. Wang, H.R. Wilson, and Y.B. Zhu. High fusion performance in Super H-mode experiments on Alcator C-Mod and DIII-D. *Nuclear Fusion*, 59(8):086017, August 2019.
- [13] E. Viezzer, M.E. Austin, M. Bernert, K.H. Burrell, P. Cano-Megias, X. Chen, D.J. Cruz-Zabala, S. Coda, M. Faitsch, O. Février, L. Gil, C. Giroud, T. Happel, G.F. Harrer, A.E. Hubbard, J.W. Hughes, A. Kallenbach, B. Labit, A. Merle, H. Meyer, C. Paz-Soldan, P. Oyola, O. Sauter, M. Siccino, D. Silvagni, and E.R. Solano. Prospects of core-edge integrated no-ELM and small-ELM scenarios for future fusion devices. *Nuclear Materials and Energy*, 34:101308, March 2023.
- [14] J. W. Hughes, B. LaBombard, D. A. Mossessian, A. E. Hubbard, J. Terry, T. Biewer, and The Alcator C-Mod Team. Advances in measurement and modeling of the high-confinement-mode pedestal on the Alcator C-Mod tokamak. *Physics of Plasmas*, 13(5):056103, May 2006.
- [15] S. Mordijck. Overview of density pedestal structure: role of fueling versus transport. *Nuclear Fusion*, 60(8):082006, August 2020.
- [16] M. A. Mahdavi, R. Maingi, R. J. Groebner, A. W. Leonard, T. H. Osborne, and G. Porter. Physics of pedestal density profile formation and its impact on H-mode density limit in burning plasmas. *Physics of Plasmas*, 10(10):3984–3991, October 2003.
- [17] R. J. Groebner, M. A. Mahdavi, A. W. Leonard, T. H. Osborne, G. D. Porter, R. J. Colchin, and L. W. Owen. The role of neutrals in high-mode (H-mode) pedestal formation. *Physics of Plasmas*, 9(5):2134–2140, May 2002.
- [18] J.W. Hughes, B. LaBombard, J. Terry, A. Hubbard, and B. Lipschultz. Edge profile stiffness and insensitivity of the density pedestal to neutral fuelling in Alcator C-Mod edge transport barriers. *Nuclear Fusion*, 47(8):1057–1063, August 2007.
- [19] B. LaBombard, J. W. Hughes, N. Smick, A. Graf, K. Marr, R. McDermott, M. Reinke, M. Greenwald, B. Lipschultz, J. L. Terry, D. G. Whyte, S. J. Zweben, and Alcator C-Mod Team. Critical gradients and plasma flows in the edge plasma of Alcator C-Mod. *Physics of Plasmas*, 15(5):056106, May 2008.
- [20] B. LaBombard, J.W. Hughes, D. Mossessian, M. Greenwald, B. Lipschultz, J.L. Terry, and The Alcator C-Mod Team. Evidence for electromagnetic fluid drift turbulence controlling the edge plasma state in the Alcator C-Mod tokamak. *Nuclear Fusion*, 45(12):1658–1675, December 2005.

- [21] J.W. Hughes, P.B. Snyder, J.R. Walk, E.M. Davis, A. Diallo, B. LaBombard, S.G. Baek, R.M. Churchill, M. Greenwald, R.J. Groebner, A.E. Hubbard, B. Lipschultz, E.S. Marmar, T. Osborne, M.L. Reinke, J.E. Rice, C. Theiler, J. Terry, A.E. White, D.G. Whyte, S. Wolfe, and X.Q. Xu. Pedestal structure and stability in H-mode and I-mode: a comparative study on Alcator C-Mod. *Nuclear Fusion*, 53(4):043016, April 2013.
- [22] M. Faitsch, T. Eich, G.F. Harter, E. Wolfrum, D. Brida, P. David, M. Dunne, L. Gil, B. Labit, and U. Stroth. Analysis and expansion of the quasi-continuous exhaust (QCE) regime in ASDEX Upgrade. *Nuclear Fusion*, 63(7):076013, July 2023.
- [23] B. LaBombard, M.V. Umansky, R.L. Boivin, J.A. Goetz, J. Hughes, B. Lipschultz, D. Mossessian, C.S. Pitcher, J.L. Terry, and Alcator Group. Cross-field plasma transport and main-chamber recycling in diverted plasmas on Alcator C-Mod. *Nuclear Fusion*, 40(12):2041–2060, December 2000.
- [24] K. Lackner and R. Schneider. The role of edge physics and confinement issues in the fusion reactor. *Fusion Engineering and Design*, 22(10):107–116, March 1993.
- [25] M. Greenwald, A. Bader, S. Baek, M. Bakhtiari, H. Barnard, W. Beck, W. Bergerson, I. Bespamyatnov, P. Bonoli, D. Brower, D. Brunner, W. Burke, J. Candy, M. Churchill, I. Cziegler, A. Diallo, A. Dominguez, B. Duval, E. Edlund, P. Ennever, D. Ernst, I. Faust, C. Fiore, T. Fredian, O. Garcia, C. Gao, J. Goetz, T. Golfopoulos, R. Granetz, O. Grulke, Z. Hartwig, S. Horne, N. Howard, A. Hubbard, J. Hughes, I. Hutchinson, J. Irby, V. Izzo, C. Kessel, B. LaBombard, C. Lau, C. Li, Y. Lin, B. Lipschultz, A. Loarte, E. Marmar, A. Mazurenko, G. McCracken, R. McDermott, O. Meneghini, D. Mikkelsen, D. Mossessian, R. Mumgaard, J. Myra, E. Nelson-Melby, R. Ochoukov, G. Olynik, R. Parker, S. Pitcher, Y. Podpaly, M. Porkolab, M. Reinke, J. Rice, W. Rowan, A. Schmidt, S. Scott, S. Shiraiwa, J. Sierchio, N. Smick, J. A. Snipes, P. Snyder, B. Sorbom, J. Stillerman, C. Sung, Y. Takase, V. Tang, J. Terry, D. Terry, C. Theiler, A. Tronchin-James, N. Tsujii, R. Vieira, J. Walk, G. Wallace, A. White, D. Whyte, J. Wilson, S. Wolfe, G. Wright, J. Wright, S. Wukitch, and S. Zweben. 20 years of research on the Alcator C-Mod tokamak. *Physics of Plasmas*, 21(11):110501, November 2014.
- [26] J.W. Hughes, P.B. Snyder, M.L. Reinke, B. LaBombard, S. Mordijck, S. Scott, E. Tolman, S.G. Baek, T. Golfopoulos, R.S. Granetz, M. Greenwald, A.E. Hubbard, E. Marmar, J.E. Rice, A.E. White, D.G. Whyte, T. Wilks, and S. Wolfe. Access to pedestal pressure relevant to burning plasmas on the high magnetic field tokamak Alcator C-Mod. *Nuclear Fusion*, 58(11):112003, November 2018.
- [27] R. Reksoatmodjo, S. Mordijck, J.W. Hughes, J.D. Lore, and X. Bonnin. The role of edge fueling in determining the pedestal density in high neutral opacity Alcator C-Mod experiments. *Nuclear Materials and Energy*, 27:100971, June 2021.
- [28] A. E. Hubbard, R. L. Boivin, R. S. Granetz, M. Greenwald, J. W. Hughes, I. H. Hutchinson, J. Irby, B. LaBombard, Y. Lin, E. S. Marmar, A. Mazurenko, D. Mossessian, E. Nelson-Melby, M. Porkolab, J. A. Snipes, J. Terry, S. Wolfe, S. Wukitch, B. A. Carreras, V. Klein, and T. Sunn Pedersen. Pedestal profiles and fluctuations in C-Mod enhanced D-alpha H-modes. *Physics of Plasmas*, 8(5):2033–2040, May 2001.
- [29] ITER Physics Expert Group on Confinement, Transport, ITER Physics Expert Group on Confinement Modelling, Database, and ITER Physics Basis Editors. Chapter 2: Plasma confinement and transport. *Nuclear Fusion*, 39(12):2175, dec 1999.
- [30] J.W. Hughes, P.B. Snyder, M.L. Reinke, B. LaBombard, S. Mordijck, S. Scott, E. Tolman, S.G. Baek, T. Golfopoulos, R.S. Granetz, M. Greenwald, A.E. Hubbard, E. Marmar, J.E. Rice, A.E. White, D.G. Whyte, T. Wilks, and S. Wolfe. Access to pedestal pressure relevant to burning plasmas on the high magnetic field tokamak alcator c-mod. *Nuclear Fusion*, 58(11):112003, sep 2018.
- [31] S. Ding, A. M. Garofalo, H. Q. Wang, D. B. Weisberg, Z. Y. Li, X. Jian, D. Eldon, B. S. Victor, A. Marinoni, Q. M. Hu, I. S. Carvalho, T. Odstrčil, L. Wang, A. W. Hyatt, T. H. Osborne, X. Z. Gong, J. P. Qian, J. Huang, J. McClenaghan, C. T. Holcomb, and J. M. Hanson. A high-density and high-confinement tokamak plasma regime for fusion energy. *Nature*, 629(8012):555–560, May 2024.
- [32] D. J. Campbell, A. Loarte, D. Boilson, X. Bonnin, P. de Vries, L. Giancarli, Y. Gribov, M. Henderson, S. H. Kim, Ph. Lamalle, M. Lehnen, T. Luce, I. Nunes, A. R. Polevoi, S. D. Pinches, R. A. Pitts, R. Reichle, M. Schneider, and J. Snipes. ITER Research Plan within the Staged Approach (Level III - Final Version). 2024.
- [33] J. W. Hughes, N. T. Howard, P. Rodriguez-Fernandez, A. J. Creely, A. Q. Kuang, P. B. Snyder, T. M. Wilks, R. Sweeney, and M. Greenwald. Projections of H-mode access and edge pedestal in the SPARC tokamak. *Journal of Plasma Physics*, 86(5):865860504, October 2020.
- [34] S. Mordijck, R.A. Chaban, R. Reksoatmodjo, J.J. Balbin-Arias, Y. Chuang, J. Loughran, J.W. Hughes, A.M. Rosenthal, M.A. Miller, T. Wilks, F.M. Laggner, and T. Osborne. Impact of ionization and transport on pedestal density structure in DIII-D and Alcator C-Mod. *Nuclear Fusion*, 64(12):126034, December 2024.
- [35] R. L. Boivin, J. A. Goetz, A. E. Hubbard, J. W. Hughes, I. H. Hutchinson, J. H. Irby, B. LaBombard, E. S. Marmar, D. Mossessian, C. S. Pitcher, J. L. Terry, B. A. Carreras, and L. W. Owen. Effects of neutral particles on edge dynamics in Alcator C-Mod plasmas. *Physics of Plasmas*, 7(5):1919–1926, May 2000.
- [36] R.L. Boivin, J. Goetz, A. Hubbard, J.W. Hughes, J. Irby, B. LaBombard, E. Marmar, D. Mossessian, and J.L. Terry. High resolution measurements of neutral density and ionization rate in the main chamber of the Alcator C-Mod tokamak. *Journal of Nuclear Materials*, 290-293:542–545, March 2001.
- [37] A. M. Rosenthal, J. W. Hughes, A. Bortolon, F. M. Laggner, T. M. Wilks, R. Vieira, R. Leccacorvi, E. Marmar, A. Nagy, C. Freeman, and D. Mauzey. A 1D Lyman-alpha profile camera for plasma edge neutral studies on the DIII-D tokamak. *Review of Scientific Instruments*, 92(3):033523, March 2021.
- [38] T. Odstrčil, T. Pütterich, M. Odstrčil, A. Gude, V. Igochine, U. Stroth, and ASDEX Upgrade Team. Optimized tomography methods for plasma emissivity reconstruction at the ASDEX Upgrade tokamak. *Review of Scientific Instruments*, 87(12):123505, December 2016.
- [39] J. W. Hughes, D. A. Mossessian, A. E. Hubbard, E. S. Marmar, D. Johnson, and D. Simon. High-resolution edge Thomson scattering measurements on the Alcator C-Mod tokamak. *Review of Scientific Instruments*, 72(1):1107–1110, January 2001.
- [40] R.J. Groebner, D.R. Baker, K.H. Burrell, T.N. Carlstrom, J.R. Ferron, P. Gohil, L.L. Lao, T.H. Osborne, D.M. Thomas, W.P. West, J.A. Boedo, R.A. Moyer, G.R. McKee, R.D. Deranian, E.J. Doyle, C.L. Rettig, T.L. Rhodes, and J.C. Rost. Progress in quantifying the edge physics of the H mode regime in DIII-D. *Nuclear Fusion*, 41(12):1789–1802, December 2001.
- [41] P.C. Stangeby. *The Plasma Boundary of Magnetic Fusion Devices*. Plasma Physics Series. Institute of Physics Publishing Ltd, 2000.
- [42] D. Brunner, B. LaBombard, A.Q. Kuang, and J.L. Terry. High-resolution heat flux width measurements at reactor-level magnetic fields and observation of a unified width scaling across confinement regimes in the Alcator C-Mod tokamak. *Nuclear Fusion*, 58(9):094002, September 2018.
- [43] B. LaBombard, R. L. Boivin, M. Greenwald, J. Hughes, B. Lipschultz, D. Mossessian, C. S. Pitcher, J. L. Terry, S. J. Zweben, and Alcator Group. Particle transport in the scrape-off layer and its relationship to discharge density limit in Alcator C-Mod. *Physics of Plasmas*, 8(5):2107–2117, May 2001.
- [44] A.M. Rosenthal, J.W. Hughes, F.M. Laggner, T. Odstrčil, A. Bortolon, T.M. Wilks, and F. Sciortino. Inference of main ion particle transport coefficients with experimentally constrained neutral ionization during edge localized mode recovery on DIII-D. *Nuclear Fusion*, 63(4):042002, April 2023.
- [45] A.M. Rosenthal, J.W. Hughes, F.M. Laggner, T. Odstrčil, A. Bortolon, T.M. Wilks, S. Mordijck, M.A. Miller, and F. Sciortino. Pedestal main ion particle transport inference

- through gas puff modulation with experimental source measurements. *Nuclear Fusion*, 64(3):036006, March 2024.
- [46] F. M. Lagnier, A. Bortolon, A. M. Rosenthal, T. M. Wilks, J. W. Hughes, C. Freeman, T. Golfinopoulos, A. Nagy, D. Mauzey, M. W. Shafer, and the DIII-D Team. Absolute calibration of the Lyman- α measurement apparatus at DIII-D. *Review of Scientific Instruments*, 92(3):033522, March 2021.
- [47] M. V. Umansky, S. I. Krasheninnikov, B. LaBombard, and J. L. Terry. Comments on particle and energy balance in the edge plasma of Alcator C-Mod. *Physics of Plasmas*, 5(9):3373–3376, September 1998.
- [48] J. C. Hillesheim, J. C. DeBoo, W. A. Peebles, T. A. Carter, G. Wang, T. L. Rhodes, L. Schmitz, G. R. McKee, Z. Yan, G. M. Staebler, K. H. Burrell, E. J. Doyle, C. Holland, C. C. Petty, S. P. Smith, A. E. White, and L. Zeng. Observation of a Critical Gradient Threshold for Electron Temperature Fluctuations in the DIII-D Tokamak. *Physical Review Letters*, 110(4):045003, January 2013.
- [49] M. N. A. Beurskens, T. H. Osborne, P. A. Schneider, E. Wolfrum, L. Frassinetti, R. Groebner, P. Lomas, I. Nunes, S. Saarelma, R. Scannell, P. B. Snyder, D. Zarzoso, I. Balboa, B. Bray, M. Brix, J. Flanagan, C. Giroud, E. Giovannozzi, M. Kempenaars, A. Loarte, E. De La Luna, G. Maddison, C. F. Maggi, D. McDonald, R. Pasqualotto, G. Saibene, R. Sartori, Emilia R. Solano, M. Walsh, L. Zabeo, The DIII-D Team, The ASDEX Upgrade Team, and JET-EFDA Contributors. H-mode pedestal scaling in DIII-D, ASDEX Upgrade, and JET. *Physics of Plasmas*, 18(5):056120, May 2011.
- [50] M. G. Dunne, S. Potzel, F. Reimold, M. Wischmeier, E. Wolfrum, L. Frassinetti, M. Beurskens, P. Bilkova, M. Cavedon, R. Fischer, B. Kurzan, F. M. Lagnier, R. M. McDermott, G. Tardini, E. Trier, E. Viezzer, M. Willensdorfer, The EUROfusion MST1 Team, and The ASDEX-Upgrade Team. The role of the density profile in the ASDEX-Upgrade pedestal structure. *Plasma Physics and Controlled Fusion*, 59(1):014017, January 2017.
- [51] H. Q. Wang, H. Y. Guo, A. W. Leonard, A. L. Moser, T. H. Osborne, P. B. Snyder, E. Belli, R. J. Groebner, D. M. Thomas, J. G. Watkins, Z. Yan, and the DIII-D group. Effects of divertor geometry on H-mode pedestal structure in attached and detached plasmas in the DIII-D tokamak. *Nuclear Fusion*, 58(9):096014, September 2018.
- [52] E. Stefanikova, L. Frassinetti, S. Saarelma, A. Loarte, I. Nunes, L. Garzotti, P. Lomas, F. Rimini, P. Drewelow, U. Kruezi, B. Lomanowski, E. De La Luna, L. Meneses, M. Peterka, B. Viola, C. Giroud, C. Maggi, and JET contributors. Effect of the relative shift between the electron density and temperature pedestal position on the pedestal stability in JET-ILW and comparison with JET-C. *Nuclear Fusion*, 58(5):056010, May 2018.
- [53] L. Frassinetti, M. G. Dunne, U. Sheikh, S. Saarelma, C. M. Roach, E. Stefanikova, C. Maggi, L. Horvath, S. Pamela, E. De La Luna, E. Wolfrum, M. Bernert, P. Blanchard, B. Labit, A. Merle, L. Guimaraes, S. Coda, H. Meyer, J. C. Hillesheim, the ASDEX Upgrade Team, JET Contributors, the TCV Team, and the EUROfusion MST1 Team. Role of the pedestal position on the pedestal performance in AUG, JET-ILW and TCV and implications for ITER. *Nuclear Fusion*, 59(7):076038, July 2019.
- [54] T. Luda, C. Angioni, M. G. Dunne, E. Fable, A. Kallenbach, N. Bonanomi, P. A. Schneider, M. Siccinio, G. Tardini, P. Rodriguez-Fernandez, J. W. Hughes, N. Howard, L. Frassinetti, S. Saarelma, The Asdex Upgrade Team, The EUROfusion Mst1 Team, The Alcator C-Mod Team, and Jet Contributors. Validation of IMEP on Alcator C-Mod and JET-ILW ELMy H-mode plasmas. *Plasma Physics and Controlled Fusion*, 65(3):034001, March 2023.
- [55] T. Eich, P. Manz, and the ASDEX Upgrade team. The separatrix operational space of ASDEX Upgrade due to interchange-drift-Alfvén turbulence. *Nuclear Fusion*, 61(8):086017, July 2021.
- [56] P. Manz, T. Eich, and O. Grover. The power dependence of the maximum achievable H-mode and (disruptive) L-mode separatrix density in ASDEX Upgrade. *Nuclear Fusion*, 63(7):076026, July 2023.
- [57] T. Eich, P. Manz, R. J. Goldston, P. Hennequin, P. David, M. Faitsch, B. Kurzan, B. Sieglin, E. Wolfrum, the ASDEX Upgrade team, and the EUROfusion MST1 team b. Turbulence driven widening of the near-SOL power width in ASDEX Upgrade H-Mode discharges. *Nuclear Fusion*, 60(5):056016, April 2020.
- [58] S. Wiesen, D. Reiter, V. Kotov, M. Baelmans, W. Dekeyser, A. S. Kukushkin, S. W. Lisgo, R. A. Pitts, V. Rozhansky, G. Saibene, I. Veselova, and S. Voskoboinikov. The new SOLPS-ITER code package. *Journal of Nuclear Materials*, 463:480–484, August 2015.
- [59] Matthias Schmidtmayr. *Investigation of the influence of the ion heat flux on access to regimes of improved energy confinement in Alcator C-Mod*. PhD thesis, Technischen Universität Wien, 2017.
- [60] D. Brunner, B. LaBombard, R. M. Churchill, J. Hughes, B. Lipschultz, R. Ochoukov, T. D. Rognlien, C. Theiler, J. Walk, M. V. Umansky, and D. Whyte. An assessment of ion temperature measurements in the boundary of the Alcator C-Mod tokamak and implications for ion fluid heat flux limiters. *Plasma Physics and Controlled Fusion*, 55(9):095010, September 2013.
- [61] J. M. Canik, R. Maingi, V. A. Soukhanovskii, R. E. Bell, H. W. Kugel, B. P. LeBlanc, and T. H. Osborne. Measurements and 2-D modeling of recycling and edge transport in discharges with lithium-coated PFCs in NSTX. *Journal of Nuclear Materials*, 415(1):S409–S412, August 2011.
- [62] R. S. Wilcox, M. W. Shafer, and J. D. Lore. Interpretive Modeling Using SOLPS-ITER For Pumping Experiments With A Closed Divertor In DIII-D. *Proceedings of the 29th IAEA Fusion Energy Conference*, 2023.
- [63] M. Kotschenreuther, X. Liu, D. R. Hatch, S. Mahajan, L. Zheng, A. Diallo, R. Groebner, the DIII-D TEAM, J. C. Hillesheim, C. F. Maggi, C. Giroud, F. Koechl, V. Parail, S. Saarelma, E. R. Solano, A. Chankin, and JET Contributors. Gyrokinetic analysis and simulation of pedestals to identify the culprits for energy losses using ‘fingerprints’. *Nuclear Fusion*, 59(9):096001, September 2019.
- [64] A. J. Creely, M. J. Greenwald, S. B. Ballinger, D. Brunner, J. Canik, J. Doody, T. Fülöp, D. T. Garnier, R. Granetz, T. K. Gray, C. Holland, N. T. Howard, J. W. Hughes, J. H. Irby, V. A. Izzo, G. J. Kramer, A. Q. Kuang, B. LaBombard, Y. Lin, B. Lipschultz, N. C. Logan, J. D. Lore, E. S. Marmar, K. Montes, R. T. Mumgaard, C. Paz-Soldan, C. Rea, M. L. Reinke, P. Rodriguez-Fernandez, K. Särkimäki, F. Sciortino, S. D. Scott, A. Snicker, P. B. Snyder, B. N. Sorbom, R. Sweeney, R. A. Tinguely, E. A. Tolman, M. Umansky, O. Vallhagen, J. Varje, D. G. Whyte, J. C. Wright, S. J. Wukitch, J. Zhu, and the SPARC Team. Overview of the SPARC tokamak. *Journal of Plasma Physics*, 86(5):865860502, October 2020.
- [65] P. Vondracek, R. Panek, M. Hron, J. Havlicek, V. Weinzettl, T. Todd, D. Tskhakaya, G. Cunningham, P. Hacek, J. Hromadka, P. Junek, J. Krbec, N. Patel, D. Sestak, J. Varju, J. Adamek, M. Balazsova, V. Balner, P. Barton, J. Bielecki, P. Bilkova, J. Blocki, D. Bocian, J. Bogar, O. Bogar, P. Boocz, I. Borodkina, A. Brooks, P. Bohm, J. Burant, A. Casolari, J. Cavalier, P. Chappuis, R. Dejarnac, M. Dimitrova, M. Dudak, I. Duran, R. Ellis, S. Entler, J. Fang, M. Farnik, O. Ficker, D. Fridrich, S. Fukova, J. Gerardin, I. Hanak, A. Havranek, A. Herrmann, J. Horacek, O. Hronova, M. Imrisek, N. Isernia, F. Jaulmes, M. Jerab, V. Kindl, M. Komm, K. Kovarik, M. Kral, L. Kripner, E. Macusova, T. Majer, T. Markovic, E. Matveeva, K. Mikszuta-Michalik, M. Mohelnik, I. Mysiura, D. Naydenkova, I. Nemec, R. Ortwein, K. Patocka, M. Peterka, A. Podolnik, F. Prochazka, J. Prevratil, J. Reboun, V. Scalera, M. Scholz, J. Svoboda, J. Swierblewski, M. Sos, M. Tadros, P. Titus, M. Tomes, A. Torres, G. Tracz, P. Turjanica, M. Varavin, V. Veselovsky, F. Villone, P. Wąchal, V. Yanovskiy, G. Zadviitskiy, J. Zajac, A. Zak, D. Zaloga, J. Zelds, and H. Zhang. Preliminary design of the COMPASS upgrade tokamak. *Fusion Engineering and Design*, 169:112490, August 2021.
- [66] B. N. Sorbom, J. Ball, T. R. Palmer, F. J. Mangiarotti, J. M. Sierchio, P. Bonoli, C. Kasten, D. A. Sutherland, H. S. Barnard,

- C.B. Haakonsen, J. Goh, C. Sung, and D.G. Whyte. ARC: A compact, high-field, fusion nuclear science facility and demonstration power plant with demountable magnets. *Fusion Engineering and Design*, 100:378–405, November 2015.
- [67] J.L. Terry, N.P. Basse, I. Cziegler, M. Greenwald, O. Grulke, B. LaBombard, S.J. Zweben, E.M. Edlund, J.W. Hughes, L. Lin, Y. Lin, M. Porkolab, M. Sampsell, B. Veto, and S.J. Wukitch. Transport phenomena in the edge of Alcator C-Mod plasmas. *Nuclear Fusion*, 45(11):1321–1327, November 2005.
- [68] O. E. Garcia, S. M. Fritzner, R. Kube, I. Cziegler, B. LaBombard, and J. L. Terry. Intermittent fluctuations in the Alcator C-Mod scrape-off layer. *Physics of Plasmas*, 20(5):055901, May 2013.
- [69] Y. R. Martin, T. Takizuka, and The Itpa Cdbm H-mode Threshold Data Group. Power requirement for accessing the H-mode in ITER. *Journal of Physics: Conference Series*, 123:012033, July 2008.
- [70] J.W. Hughes, A. Loarte, M.L. Reinke, J.L. Terry, D. Brunner, M. Greenwald, A.E. Hubbard, B. LaBombard, B. Lipschultz, Y. Ma, S. Wolfe, and S.J. Wukitch. Power requirements for superior H-mode confinement on Alcator C-Mod: experiments in support of ITER. *Nuclear Fusion*, 51(8):083007, August 2011.
- [71] Y. Ma, J.W. Hughes, A.E. Hubbard, B. LaBombard, R.M. Churchill, T. Golfinopolous, N. Tsujii, and E.S. Marmar. Scaling of H-mode threshold power and L–H edge conditions with favourable ion grad-B drift in Alcator C-Mod tokamak. *Nuclear Fusion*, 52(2):023010, February 2012.
- [72] D. Moulton, P.C. Stangeby, X. Bonnin, and R.A. Pitts. Comparison between SOLPS-4.3 and the Lengyel Model for ITER baseline neon-seeded plasmas. *Nuclear Fusion*, 61(4):046029, March 2021.
- [73] S.B. Ballinger, A.Q. Kuang, M.V. Umansky, D. Brunner, J.M. Canik, M. Greenwald, J.D. Lore, B. LaBombard, J.L. Terry, M. Wigram, and The Sparc Team. Simulation of the SPARC plasma boundary with the UEDGE code. *Nuclear Fusion*, 61(8):086014, August 2021.
- [74] P. Rodriguez-Fernandez, N. T. Howard, A. Saltzman, L. Shoji, T. Body, D. J. Battaglia, J. W. Hughes, J. Candy, G. M. Staebler, and A. J. Creely. Core performance predictions in projected SPARC first-campaign plasmas with nonlinear CGYRO, March 2024. arXiv:2403.15633 [physics].
- [75] A. Q. Kuang, S. Ballinger, D. Brunner, J. Canik, A. J. Creely, T. Gray, M. Greenwald, J. W. Hughes, J. Irby, B. LaBombard, B. Lipschultz, J. D. Lore, M. L. Reinke, J. L. Terry, M. Umansky, D. G. Whyte, S. Wukitch, and the SPARC Team. Divertor heat flux challenge and mitigation in SPARC. *Journal of Plasma Physics*, 86(5):865860505, October 2020.
- [76] A.W. Leonard, A. Herrmann, K. Itami, J. Lingertat, A. Loarte, T.H. Osborne, W. Suttrop, The Iter Divertor Modeling Database Expert Group, , and The Iter Divertor Physics Expert Group. The impact of ELMs on the ITER divertor. *Journal of Nuclear Materials*, 266-269:109–117, March 1999.
- [77] T. Eich, P. Manz, R. J. Goldston, P. Hennequin, P. David, M. Faitsch, B. Kurzan, B. Sieglin, and E. Wolfrum. Turbulence driven widening of the near-SOL power width in ASDEX Upgrade H-Mode discharges. *Nucl. Fusion*, 2020.
- [78] M. Faitsch, T. Eich, G.F. Harrer, E. Wolfrum, D. Brida, P. David, M. Griener, and U. Stroth. Broadening of the power fall-off length in a high density, high confinement H-mode regime in ASDEX Upgrade. *Nuclear Materials and Energy*, 26:100890, March 2021.